TITLE: Fine-tuned repression of Drp1 driven mitochondrial fission primes a slow cycling stem/progenitor-like state towards accelerating neoplastic transformation of keratinocytes

AUTHORS: Spurlock B[1], Parker D[1], Basu MK[2], Hjelmeland A[3], G Sajina[3], Liu S[1], Siegal G[2], Gunter A[1], Moran A[1] and Mitra K[1]*

* corresponding author (kasturi@uab.edu)

AFFILIATION:

1. Department of Genetics, University of Alabama at Birmingham, Birmingham, Alabama 35294
2. Department of Pathology, University of Alabama at Birmingham, Birmingham, Alabama 35294
3. Department of Cell Development and Integrative Biology, University of Alabama at Birmingham,
4. Department of Biology, University of Alabama at Birmingham.

Running title:
Mitochondria based priming of stem/progenitor-like state towards driving transformation

Keywords:
Drp1, Mitochondrial fission, neoplastic stem/progenitor cells, neoplastic transformation, keratinocytes, scRNA-seq, microscopy

ABSTRACT:

The opposing processes of mitochondrial fission and fusion are emerging as crucial regulators of stem cells. Stem/progenitor cells maintaining repressed mitochondrial fission appear to be primed for self-renewal and proliferation. Here, we demonstrate the causative role of fine-tuned repression of Drp1, the master regulator of mitochondrial fission, in establishing a stem/progenitor-like state towards supporting carcinogen (TCDD) driven neoplastic transformation of keratinocytes. Fine-tuned Drp1 repression maintains small networks of fused mitochondria to sustain a unique gene-expression profile with elevated stem/progenitor cell functional markers (Krt15, Sox2 etc) and their regulators (Cyclin E). Cells with this mitochondria-primed state are slow cycling, susceptible to transformation, and when enriched by mild carcinogen exposure sustains elevated self-renewal/proliferation to form less differentiated tumors. More complete Drp1 repression sustains larger hyperfused mitochondria, represses lineage specific stem/progenitor genes and prevents transformation. Therefore, our data highlights a 'goldilocks' level of Drp1 repression that supports stem/progenitor cell dependent neoplastic transformation. Future studies would reveal if bodily stresses causing mild Drp1 repression could enrich this mitochondria-primed stem/progenitor like population in tissues making them vulnerable to neoplastic transformation.

INTRODUCTION

Mitochondria play various key roles in stem cell regulation, while their involvement is complex (Lisowski, Kannan et al., 2018)(Khacho & Slack, 2017, Zhang, Menzies et al., 2018). The critical details of mitochondrial involvement in regulation of various stem cell properties are far from clear. The master regulators of mitochondrial fission and fusion processes are emerging as crucial regulators of both embryonic and adult stem cells (Khacho & Slack, 2017, Lisowski et al., 2018)(Spurlock, Tullet et al., 2020). The Dynamin Related Protein 1 (Drp1) is the master regulator of mitochondrial fission that breaks larger mitochondria into smaller elements(Friedman & Nunnari, 2014, Kageyama, Zhang et al., 2011). The effects of Drp1 driven mitochondrial fission is opposed by fusion between mitochondria driven by the Mitofusins and Opa1(Chen & Chan, 2017)(Schrepfer & Scorrano, 2016). Therefore, Drp1 repression allows unopposed mitochondrial fusion to sustain a hyperfused mitochondrial state. The other extreme state, i.e. unopposed mitochondrial fission, is critical for achieving pluripotency of stem cells during reprogramming (Prieto, Leon et al., 2016). However, sustained mitochondrial fission reduces pluripotency of stem cells (Zhong, Cui et al., 2019). Thus, a balance of timely fission and fusion of mitochondria appears to be critical for maintaining stem cell properties.

Enhanced mitochondrial fusion sustains stemness of certain adult stem cells of neural, germ line and mammary lineages (Khacho, Clark et al., 2016, Senos Demarco, Uyemura et al., 2019, Wu, Chen et al., 2019). Particularly, repression of Drp1 supports stemness and repression of Mitofusin or Opa1 inactivates stemness in adult mouse neural lineage (Iwata, Casimir et al., 2020, Khacho & Slack, 2017). In various tumors, the bulk tumor cell populations are maintained by the adult neoplastic stem cells (also called tumor initiating cells) as they self-renew, proliferate and differentiate (Magee, Piskounova et al., 2012). Drp1 has been linked to tumor formation in various cancer types (Nagdas, Kashatus et al., 2019, Serasinghe, Wieder et al., 2015, Tanwar, Parker et al., 2016, Tsuyoshi, Orisaka et al., 2020, Xie, Wu et al., 2015). Drp1 activation sustains neoplastic stem cells at least in the astrocytic lineage (Xie et al., 2015). Although various mechanisms and pathways have been proposed towards modulation

of stem cell properties by mitochondrial fission and fusion regulators, no common theme has yet emerged.

Given that stem cells exhibit plasticity at various levels, a detailed understanding of various states of these cells is an important area of investigation (Magee, Piskounova et al., 2012)(Folmes, Dzeja et al., 2012). We found that select neoplastic ovarian epithelial stem cells (marked by Aldh) have lower levels of mitochondrial fission and can convert to a state of elevated mitochondrial fission when self-renewal and proliferation is activated (Spurlock et al., 2019)(Spurlock et al., 2021b). Importantly, the cells with minimum mitochondrial fission were found within a neoplastic stem cell sub-population that has >10 folds self-renewal and proliferation ability compared to the other neoplastic stem cell subpopulation (Spurlock et al., 2019)(Spurlock et al., 2021b). Thus, we proposed, that a repressed mitochondrial fission state may prime neoplastic stem cells towards maximizing their potential of self-renewal and proliferation. Similar priming was demonstrated in a normal hematopoietic stem cell subpopulation that maintains Drp1 repression (Liang, Arif et al., 2020). However, the causative role of Drp1 in mitochondria driven priming of stem cell self-renewal/proliferation remains to be investigated. Nonetheless, an elevated mitochondrial fusion state, sustained by mitofusin, was shown to drive immortalization of neoplastic stem cells to support tumorigenesis in a Drosophila model (Bonnay, Veloso et al., 2020). Therefore, it is important to study the detailed involvement of mitochondrial fission and fusion in the mitochondria based priming of stem cell self-renewal and proliferation.

Here, we investigated involvement of Drp1 in mitochondria based priming of stemness during neoplastic transformation of skin cells. Skin stem cells sustain the regenerative capacity of the organ and thus serve as an excellent model for adult stem cells (Fuchs, 2016), while the role of Drp1 remains largely unknown in this system. Therefore, we took the first step of detailed investigation of the spontaneously immortalized skin keratinocyte cell line, HaCaT, which has been widely used to model the basic organization of skin and how carcinogens impact it (Boelsma, Verhoeven et al., 1999, Jung, Jung et al., 2016, Schoop, Mirancea et al., 1999). The HaCaT cells carry a non-functional p53 (St John, Sauter et al., 2000), which provides the appropriate cellular context given Drp1 inactivation increases cell proliferation in the absence of

active p53 (Mitra, Rikhy et al., 2012, Mitra, Wunder et al., 2009). Here, we tested if Drp1 repression is involved in mitochondria based priming of stem cells towards driving neoplastic transformation.

RESULTS AND DISCUSSION

Keratinocytes transformed under mild carcinogenic stress exhibit attenuated Drp1 activity and have abundant self-renewing/proliferating cells

The potent carcinogenic impact of the chemical carcinogen 2,3,7,8-tetrachlorodibenzodioxin (TCDD), an environmental pollutant, has been widely studied on the HaCaT line as well as on skin tissue (Wincent, Bengtsson et al., 2012)(Hao, Lee et al., 2012)(Ray & Swanson, 2004)(Mulero-Navarro & Fernandez-Salguero, 2016)(Der Vartanian, Quetin et al., 2019). We used both mild and strong dose of TCDD to uncover any possibility of mitochondria based stemness priming during TCDD driven neoplastic transformation. TCDD driven carcinogenesis is largely caused by activation and upregulation of the aryl hydrocarbon receptor (AHR) (Mulero-Navarro & Fernandez-Salguero, 2016) (Leclerc, Staats Pires et al., 2021). Exposure to milder (T-1nM) and stronger (T-10nM) doses of TCDD causes a comparable increase in cell proliferation of HaCaT cells within 3 weeks of standard TCCD driven transformation protocol, with Toluene used as the vehicle control (Fig. 1A). The stable transformed colonies of TCDD-1nM (TF-1) and TCDD-10nM (TF-10) maintain comparable upregulation of AHR, even in the absence of TCDD (Fig. 1B). Unlike the parental HaCaT cells (Parental), both transformed cells are able to form subcutaneous xenograft tumors, confirming their transformation status (Extended. Fig. 1A). Interestingly, pathological evaluation of H&E stained tumor sections revealed that the TF-1 cells gave rise to malignant tumors harboring less differentiated (primitive) squamous cells with large nuclei (blue) and little visible cytoplasm (pink) (Fig. 1C, left). Whereas the TF-10 cells formed tumors harboring differentiated stratified squamous epithelium with cells having expansion of cytoplasm (Fig. 1C, right); the clear gaps represent artifacts secondary to cryo-sectioning.

155 Given the above differences between the TF-1 and TF-10 populations, we
156 probed for any difference in Drp1 and mitochondrial shape, as well as self-renewal and
157 proliferation abilities between them and the non-transformed Parental population.
158 Among the major molecules regulating mitochondrial fission and fusion (Drp1, Mfn1,
159 Mfn2, Opa1), Drp1 exhibited the most prominent differences (Fig. 1D). Particularly, the
160 TF1 population has markedly lower levels of the cell cycle regulated activating
161 phosphorylation of Drp1 (pDrp1-S616), while both the transformed populations have
162 higher levels of Drp1 protein compared to the Parental line (Fig. 1D). The TF-1
163 population also has lower levels of other tested mitochondrial markers (Tom20,
164 Cytochrome C and Fis1), compared to the TF-10 population (Extended Fig. 1B). Next,
165 to assess the steady state contribution of mitochondrial fission and fusion on
166 mitochondrial shape we quantified mitochondrial [Fission] and [Fusion5] metrics in
167 individual live cells stably expressing the fluorescent mitochondrial reporter, mitoPSmO
168 (Spurlock et al., 2019)(Spurlock et al., 2021b) (Fig. 1E). In comparison to the TF-1 and
169 Parental populations, the TF-10 population exhibits reduced levels of the [Fusion5]
170 metric and slightly elevated level of the [Fission] metric (Fig. 1F). Notably, although the
171 TF-1 population has higher median [Fusion5], lower range of [Fusion5] is also detected
172 in this population (Fig. 1F). Since the [Fusion5] metric reflects mitochondrial length in
173 each cell (Spurlock et al., 2019), this data suggests a wider range of mitochondrial
174 length in the TF-1 population, which could be potentially brought about by regulating
175 Drp1 driven mitochondrial fission (Fig. 1D).
176 Drp1 repression brings about a p53 dependent cell cycle block (Mitra et al.,
177 2009), and can increase cell proliferation in the absence of functional p53 (Parker, Iyer
178 et al., 2015)(Mitra et al., 2012). Consistent with this, the TF-1 HaCaT population with
179 inactive p53 status (St John et al., 2000) and low levels of active Drp1 (Fig. 1D) have
180 significantly higher *in vitro* cell proliferation rate, compared to the Parental and the TF-
181 10 population (Fig 1G). Furthermore, the TF-1 population form markedly larger
182 spheroids in conditions that support self-renewal and proliferation, in comparison to
183 those formed by the Parental or the TF-10 population (Fig. 1H). More importantly, ELDA
184 statistics applied on spheroid formation assay for determination of *in vitro* stem cell
185 frequency (Hu & Smyth, 2009) demonstrated that the TF-1 population has double the

186 abundance of self-renewing/proliferating cells than the TF-10 population, while their
187 abundance is one order higher in both transformed populations compared to the
188 Parental (Fig. 1I).
189 In summary, the above data demonstrate that keratinocytes transformed with low
190 dose of the potent carcinogen, TCDD, maintain attenuated Drp1 activity ([Drp1]-att),
191 greater self-renewal/proliferative ability and form less differentiated tumors compared to
192 those transformed by a 10-fold higher TCDD dose. Thus, we conclude that the [Drp1]-
193 att TF-1 keratinocyte population is enriched in neoplastic stem/progenitor cells.
194
195 **Drp1 attenuated TF-1 keratinocyte population maintains an expanded slow-**
196 **cycling sub-population with elevated stem/progenitor cell markers**
197 Single cell methods, particularly single-cell-RNAseq (scRNA-seq), are widely
198 used to identify and characterize distinct cellular states in a given cell population
199 (Luecken & Theis, 2019). To identify and define the neoplastic stem cells of the Drp1
200 attenuated TF-1 population, we performed scRNA-seq of the Parental and the
201 transformed populations. Cell clustering in a UMAP plot shows 6 clusters within
202 Parental, TF-1 and TF-10 populations (Fig. 2A, Clusters 0-5). While Cluster 4 is reduced
203 in both transformed populations in comparison to the Parental, the TF-1 population
204 exhibits a marked expansion of Cluster 3 and reduction of Cluster 5 (Fig. 2A, Extended.
205 Fig.2A, left panel). These results also hold true with the lowest cluster resolution
206 (Extended. Fig. 2B. arrows). Heat map of cluster markers altered by at least 1.5 folds
207 (p-adjusted <0.0001) shows that Clusters 2,3 and 4 are marked by upregulation of
208 distinct genes while Cluster 5 is marked by overall downregulation of various genes
209 (Extended Fig. 2C, Extended. Data Table 1). From here, we identified the top most
210 candidate genes to mark each cluster (color coded arrows in Extended Fig. 2C). Indeed,
211 the neoplastic stem/progenitor cell enriched Drp1-att TF-1 population shows >3-fold
212 upregulation of the epidermal stem cell marker Krt15 (Giroux, Lento et al., 2017,
213 Gonzales & Fuchs, 2017, Purba, Haslam et al., 2014) and of the neoplastic stem cell
214 markers for skin carcinomas, SOX2 and SOX4 (Boumahdi, Driessens et al., 2014,
215 Foronda, Martinez et al., 2014) (Fig. 2B, arrow). Since the markers increase across all
216 TF-1 clusters, with maximum levels in Cluster 3, we conclude that the TF-1 population

217 exhibits upregulation of the stem/progenitor markers independent of their cluster
218 distribution. On the other hand, the other stem/progenitor cell markers, like Krt5, Krt14,
219 Krt19 (Gonzales & Fuchs, 2017)(Karantza, 2011) are also enriched by ~2-fold in Cluster
220 3, but comparably in all the three cell populations, as exemplified by Krt5 (Fig. 2B,
221 arrow, Extended Data Table 1). Notably, among the 3 cell populations, TF-1 harbors
222 markedly fewer cells in Cluster 3 having elevated levels of the differentiating cell marker
223 Krt13 (Karantza, 2011). Cluster 5, reduced in TF-1 population, is marked by 1.5 to >2-
224 fold reduced expression of 12 of the 13mtDNA genes in all the 3 cell populations
225 (Extended Fig. 2D, arrow). Cluster 4, reduced in both transformed populations, is
226 marked by >8-fold upregulation of OASL, a gene involved in the interferon pathway, in
227 all the three cell populations (Extended Fig. 2E).
228 Since flow cytometry on PI stained cells revealed modest differences in cell cycle
229 distribution between the Parental and transformed populations (Extended. Fig. 2A, right
230 panel), we asked if the scRNA-seq derived clusters represent distinct cell cycle phases.
231 Therefore, we performed the standard gene set enrichment analyses (GSEA) of the
232 overall cluster marker profiles using the REACTOME pathway database (Subramanian,
233 Tamayo et al., 2005) (Extended. Data Table 2). Some of the statistically significant
234 pathways (q value <0.01) were renamed based on the leading-edge genes of the
235 identified pathways. GSEA showed upregulation of genes in “Mitosis and Relevant
236 Cytoskeletal Proteins” in Cluster 2 and that of genes in “DNA repair / replication and
237 Histones” in Cluster 0 (Fig. 2C); Cluster 1 has downregulation of “Histones and Ubiquitin
238 related” genes. Indeed, the mitotic Cyclin B and its partner kinase CDK1, as well as
239 Cyclin A are markedly higher in Cluster 2-G2-M, while PCNA, which peaks early in S
240 phase (Maga & Hubscher, 2003, Zerjatke, Gak et al., 2017) is highest in Cluster 0-S-
241 Histone-hi in all 3 cell populations (Fig. 2D); the S phase cyclins E1/E2 and their partner
242 CDK2 were not detected in our sc-RNAseq data set. Surprisingly, Cluster 3 (positively
243 marked by Krt15) has dramatic downregulation of genes in “Overall Cell Cycle” as well
244 as the above categories representing distinct cell cycle phases (Fig. 2C), suggesting
245 their cell cycling is slow. This is reflected in dramatic low levels of cyclins in Cluster 3-
246 SloCycl-Krt15-hi in all three cell populations, most prominently in TF-1 (Fig. 2D). More
247 importantly, the levels of PCNA, whose transcripts are dramatically reduced in

248 quiescent cells (Maga & Hubscher, 2003, Zerjatke, Gak et al., 2017), is markedly
249 reduced in the SloCycl-Krt15-hi cluster (and others) only in the TF-1 population (Fig.
250 2D). This cluster indeed has upregulation of genes involved in “Keratin” and “Signaling”
251 pathways. Notably, the Notch pathway target, Hes1, which actively maintains
252 quiescence (Sang, Coller et al., 2008) (Moriyama, Durham et al., 2008), is upregulated
253 across the clusters in the TF-1 population (Extended Fig. 2E). These data strongly
254 suggest that the enrichment of the SloCycl-Krt15-hi cluster in the TF-1 population
255 happens due to active maintenance of quiescence, rendering them slow cycling. Cluster
256 4 does not relate to cell cycle and shows upregulation of genes related to “Cytokine”
257 (interferons) pathway (Fig. 2C), many of which are suppressed by AHR activation (Di
258 Meglio, Duarte et al., 2014) (Extended. Data Table 1). Thus, comparable upregulation of
259 AHR in both transformed populations (Fig. 1B) could explain their comparable reduction
260 of Cluster 4 (Fig. 2A). The downregulated mtDNA genes in Cluster 5 were identified as
261 “TCA cycle” and “Complex 1 biogenesis” in our overrepresentation analyses (* in Fig.
262 2C), but not in GSEA. Towards understanding the entry into the slow cycling state of the
263 Krt15hi-Cluster 3, we performed trajectory analyses using Slingshot algorithm that
264 identifies clusters related to each other based on their gene expression (Street *et al*,
265 2018). The output trajectory was the following: “G2-M” to “S-Histones-hi” to “Cytokine”
266 to “Histones/Ub-lo” bifurcating into “SloCycl-Krt15-hi” or “mtDNA-lo” (Fig. 2C, open
267 arrows, Extended. Fig. 2F). This implies that the cells in the TF-1 population may
268 preferentially reside in the SloCycl-Krt15-hi cluster and not in the mtDNA-lo cluster, thus
269 expanding the former and reducing the latter (Fig. 2A).
270 Given the above striking differences in cell cycle genes between the clusters, we
271 quantified cell cycle distribution in each cluster in the Parental, TF-1 and TF-10
272 populations. We used a Seurat algorithm that employs several validated predictive cell
273 cycle genes to quantify G2-M and S scores, and assign cells in G2-M, S or in G1/G0
274 (when both G2-M and S phase scores are low) (Tirosh *et al*, 2016). We found that the
275 G2-M score is overall comparable between Parental and the transformed populations,
276 while the TF-1 population has lower S score (Fig. 2E). Distribution of cell cycle phase
277 across the clusters indeed corroborated the major conclusions from GSEA, namely
278 Cluster 2 is abundant in G2-M cells, Cluster 0 (and 1) in S and Krt15 marked Cluster 3

279 is in G0/G1 (expected for quiescent/slow-cycling cells) (Fig. 2F,G). This data, taken with
280 the lower levels of Histone transcripts in Cluster 1 than in Cluster 0 (* in Fig. Extended
281 2C) suggest that Cluster 0 is early S phase while Cluster 1 is late S phase. While the
282 G2-M and S cells are equally abundant in all three cell populations, the expanded
283 SloCycl-Krt15-hi cluster in the TF-1 population has significantly more cells in G0/G1 and
284 less cells in S than the other two populations (Fig. 2F,G, arrows). On the other hand, the
285 reduced mt-DNA-lo cluster in the TF-1 population has more cells in S and less in G0/G1
286 population (Fig. 2F,G, arrows). Quantification of this reciprocal relationship of G1 and S
287 distribution between Cluster 3 and 5 revealed that the G1 to S reciprocity between
288 Cluster 3 and 5 is >5-fold in the TF-1 population with respect to the Parental and TF-10
289 population (Fig. 2G, inset). This suggests that altered cell cycle regulation in the TF-1
290 population may allow them to preferentially reside in the 3-SloCycl-Krt15-hi cluster and
291 not in the 5-mtDNA-lo cluster. Such a regulation may involve attenuation of CDK1
292 driven Drp1(S616) phosphorylation (Fig. 1D) due to marked reduction of CyclinB/CDK1
293 particularly in the TF-1 population in late S phase (Fig. 2D), where decision for
294 expansion of the slow cycling Krt15-hi cluster is likely made (Fig. 2C, Suppl Fig. 2F).
295 In summary, our sc-RNAseq data demonstrate that the [Drp1]-att TF-1
296 keratinocyte population enriched with self-renewing cells maintain an expansion of slow
297 cycling cells expressing high levels of stem/progenitor markers Krt15 (lineage specific)
298 and Sox2 and Sox4 (general), likely due to altered cell cycle regulation. Consistent with
299 our data, the Krt15+ epidermal stem cells are primarily slow cycling and when activated
300 give rise to various epithelial cell types or contribute to epidermal carcinoma
301 development (Giroux et al., 2017, Gonzales & Fuchs, 2017, Purba et al., 2014)(Morris,
302 Liu et al., 2004)(Giroux et al., 2017). Moreover, the higher *in vitro* cell proliferation rate
303 of the [Drp1]-att TF-1 keratinocytes (Fig. 1G) could result from the higher clonogenic
304 capacity of the Krt15-hi cells (Morris et al., 2004)(Seykora & Cotsarelis, 2011).
305

306 **Fine-tuned repression of Drp1 sustains a [CyclinE^{hi}-Sox2^{hi}-Krt15^{hi}] state and**
307 **accelerates carcinogen driven cell transformation**

308 Repression of Drp1 driven mitochondrial fission elevates stem/progenitor cell
309 markers in mouse embryonic fibroblasts, and in cells of neural and ovarian epithelial

310 lineage (Iwata et al., 2020, Parker et al., 2015). In the epidermal lineage, Krt15+ self-
311 renewing stem cells contribute to both skin regeneration and carcinoma development
312 (Giroux et al., 2017, Gonzales & Fuchs, 2017, Purba et al., 2014), while Sox2
313 upregulation in neoplastic stem/progenitor cells particularly supports skin carcinoma
314 (Boumahdi et al., 2014, Siegle, Basin et al., 2014). We found that, in comparison to the
315 Parental and TF-10 keratinocyte populations, Sox2 protein levels are dramatically
316 higher in the Drp1 attenuated TF-1 population (Fig. 3A, Extended Fig. 3A), which are
317 enriched for self-renewing cells, have higher in vitro cell proliferation rate and forms less
318 differentiated tumors (Fig. 1). This also corroborates the elevated Sox2 transcript level
319 seen across the scRNA-seq derived clusters in the TF-1 population (Fig. 2B). Krt15
320 protein levels are elevated in both transformed populations in comparison to the
321 Parental (Fig. 3A), unlike the cluster specific differences in transcript levels (Fig. 2B).
322 We did not detect any increase in other embryonic stem cell markers like Oct4 or Nanog
323 in the TF-1 population (Extended Fig. 3A). Immunostaining based co-expression
324 analyses of Sox2 and Krt15 in individual cells revealed that only a subpopulation of
325 Drp1 attenuated TF-1 population has elevation of both Krt15 and Sox2 (Fig. 3B,
326 Extended. Fig. 3B). Similar analyses showed that the highest levels of Sox2 in the TF-1
327 population is sustained in cells with an intermediate level of Drp1 protein levels (Fig. 3C)
328 and lower pDrp1(S616) levels (indicative of lower Drp1 activity) (Fig. 3D). Therefore, we
329 investigated whether repression of Drp1 in the Parental cells may cause the elevation of
330 Sox2 and/or Krt15 observed in the TF-1 population derived from the Parental cells (with
331 carcinogen treatment). To that end, we knocked down Drp1 expression in Parental
332 keratinocytes with two validated Drp1 shRNAs (Parker et al., 2015, Tanwar et al., 2016),
333 one weaker (W), and the other with 5 folds stronger Drp1 knockdown efficacy (S) almost
334 mimicking Drp1 genetic ablation (Fig. 3E). Surprisingly, while weaker Drp1 knockdown
335 elevates Krt15 levels, while the stronger Drp1 knockdown fails to do so (Fig. 3E). On the
336 other hand, both weak and strong Drp1 knockdown caused marked elevation of Sox2 in
337 a graded fashion (Fig. 3E). The increase in Sox2 with Drp1 repression in the
338 keratinocytes is consistent with findings in Drp1 ablated mouse embryonic fibroblasts
339 (Parker et al., 2015) and neural stem cells (Iwata et al., 2020). Thus, unlike the stronger
340 Drp1 knockdown, the weaker Drp1 knockdown maintains detectable Drp1 protein, and

341 uniquely sustains a Sox2-hi/Krt15-hi population characteristic of the naturally Drp1
342 attenuated TF-1 population.
343 Cell cycle status is a crucial determinant of stemness (Orford & Scadden, 2008,
344 Otsuki & Brand, 2018, Pauklin & Vallier, 2013). Sox2 expression is under the influence
345 of various G1 cyclins (Liu, Michowski et al., 2019). Cyclin E, which is indispensable for
346 S phase entry from quiescence and also for neoplastic transformation (Geng, Yu et al.,
347 2003, Siu, Rosner et al., 2012), is critical for sustaining Sox2 expression (Liu et al.,
348 2019). Interestingly, among the major cyclins, Cyclin E1 levels are particularly higher in
349 the Sox2 enriched Drp1 attenuated TF-1 population, when compared to the Parental,
350 while Cyclin D is particularly higher in the TF-10 population (corroborating sc-RNAseq
351 data, Fig. 2D) (Fig. 3F). Moreover, Cyclin E1 is preferentially accumulated in the
352 nucleus in the TF-1 population, which is required to impact gene expression of Sox2
353 (and others) (Fig. 3G,H). Stringent regulation the Cyclin E protein levels involves its
354 degradation triggered by phosphorylation by its cognate kinase CDK2 at the T62
355 residue (Siu et al., 2012). Thus, level of pCyclinE(T-62) reflects the level of active Cyclin
356 E that drives transcription and remains susceptible to degradation. Immunostaining
357 based co-expression analyses showed that in the TF-1 population, elevated Sox2 is
358 sustained in cells with lower level of pCyclinE(T-62) than in the Parental population that
359 has overall lower levels of Sox2 (Fig. 3I). Moreover, cycloheximide chase assay, to
360 assess degradation rate of proteins, revealed no Cyclin E degradation in TF-1 cells in
361 comparison to marked CycE degradation in the Parental cells; both populations
362 maintain Tom20 (mitochondrial marker) within the 2 hour assay time frame (Extended.
363 Fig. 3C). Thus, our data is consistent with elevated Sox2 in the TF-1 population being
364 sustained by elevated Cyclin E levels achieved by attenuation of its degradation
365 kinetics. Given, mitochondrial regulation of Cyclin E regulates Cyclin E degradation
366 (Mandal, Freije et al., 2010, Parker et al., 2015), we tested if repression of Drp1 driven
367 mitochondrial fission in the Parental cells can elevate Cyclin E levels towards sustaining
368 the observed elevated Sox2 levels. Indeed, Cyclin E is dramatically accumulated in the
369 nucleus in a graded manner with Drp1 knockdown efficacy (Fig. 3J,K), similar to Sox2
370 (Fig. 3E). Thus, our data shows that Drp1 repression elevates nuclear Cyclin E and
371 Sox2 levels, which is characteristic of the naturally Drp1 attenuated TF-1 population.

372 Given, Sox2 and Cyclin E are important for neoplastic transformation in various
373 cancer types (Hwang & Clurman, 2005, Schaefer & Lengerke, 2020, Teixeira & Reed,
374 2017), and Krt15+ cells give rise to skin carcinoma (Li, Park et al., 2013, Seykora &
375 Cotsarelis, 2011), we asked if repression of Drp1 can modulate the process of
376 carcinogen driven neoplastic transformation of keratinocytes. Thus, we exposed control
377 and Drp1 knockdown Parental keratinocytes to 1 and 10nM TCDD following standard
378 TCDD driven transformation protocol. Interestingly, the weaker Drp1 knockdown, which
379 maintains Krt15-hi/Sox2-hi status and elevated nuclear Cyclin E, got transformed by
380 10nM TCDD even earlier than the control (Fig. 3L); 1 nM TCDD did not cause any
381 transformation at this time point. This happened in spite of their lower proliferation rate
382 than the control in the earlier time point. On the other hand, the stronger Drp1
383 knockdown, which also maintained slower cell proliferation rate and a Krt15-lo/Sox2-hi
384 status with elevated nuclear Cyclin E, is not transformed in the same time window (Fig.
385 3L).
386 In summary, our data suggest that fine-tuned repression (ftr) of Drp1, sustained
387 by incomplete knockdown of Drp1, allows enrichment of a [Drp1^{ftr}-CyclinE^{hi}-Sox2^{hi}-
388 Krt15^{hi}] state that is particularly susceptible to neoplastic transformation by higher TCDD
389 dose. This primed state is characteristic of the neoplastic stem/progenitor cell enriched
390 [Drp1^{att}-CyclinE^{hi}-Sox2^{hi}-Krt15^{hi}] TF-1 population resulting with lower TCDD dose.
391 Moreover, close to complete repression of Drp1 sustains a [Drp1^{lo}-CyclinE^{hi}-Sox2^{hi}-
392 Krt15^{lo}] state, and does not support transformation as reported for Drp1 ablated MEFs
393 (Serasinghe et al., 2015).
394
395 **Fine-tuned repression of Drp1 maintains smaller fused mitochondrial elements,**
396 **and sustains transcriptomic profile similar to the neoplastic stem cell enriched**
397 **TF-1 population**
398 Towards understanding the mechanism of fine-tuned (incomplete) Drp1
399 repression driven priming of neoplastic transformation, we performed detailed
400 comparison of mitochondrial shape and over all gene expression between the Parental
401 keratinocytes expressing control, weak or strong Drp1 shRNAs. Quantification of
402 mitochondrial fission and fusion metrics contributing to mitochondrial shape in live cells

403 confirmed that the stronger (more complete) Drp1 knockdown maintains ~77% of the
404 cells in the hyperfused state i.e. [Fission] metric <0.2 and [Fusion5] metric >80
405 (Spurlock et al., 2019), while the control population maintains ~55% of the cells in this
406 state (Fig. 4A, blue box, Extended. Fig. 3D). On the other hand, the weaker
407 (incomplete) Drp1 knockdown maintains only ~40% of the cells in the hyperfused state
408 (Fig. 4A, blue box), while uniquely maintaining ~28% of the cells in the [Fission] range of
409 0.2-0.4 and [Fusion5] range of 40-80 (Fig. 4A, red box). Closer examination of cells
410 within this unique population in the weaker Drp1 knockdown population revealed distinct
411 mitochondrial fragments along with extensive tubular mitochondria, as opposed to
412 uniformly hyperfused mitochondria (Extended Fig. 3D). To understand this distribution
413 better, we probed the relationship of mitochondrial fission and fusion metrics with the
414 mitochondrial number and length metrics that they are derived from. The cells with the
415 unique mitochondrial fission/fusion state (Fission: 0.2-0.4 and Fusion5: 40-80) have
416 lower mitochondrial number and total mitochondrial length (Fig. 4B), signifying decrease
417 in mitochondrial content in this subpopulation. However, cells with hyperfused
418 mitochondria (Fission<0.2; Fusion5>80) have distinctly higher mitochondrial number in
419 the weaker Drp1 knockdown population but have comparable mitochondrial length to
420 those in the stronger Drp1 knockdown population (Fig. 4B). To confirm that such an
421 increase in mitochondrial number in the weaker Drp1 knockdown with hyperfused
422 mitochondria is due to a greater number of smaller mitochondrial hyperfused networks,
423 we quantified the percent length of the longest mitochondrial elements (Fusion1).
424 Indeed, less than 7% of cells have >80% of the mitochondrial length as hyperfused in
425 the weaker Drp1 knockdown, compared to ~40% in the stronger Drp1 knockdown (Fig.
426 4C, top). More importantly, the enriched population of cells in the weaker Drp1
427 knockdown with fission range of 0.2-0.4 have only up to 40% of the mitochondrial
428 lengths in fused networks (Fig. 4C, bottom). We detected cells with similar
429 mitochondrial fission and fusion features particularly in (FACS sorted) mitochondria
430 primed ovarian neoplastic stem cell population that has 10-fold higher ability of self-
431 renewal and proliferation (Spurlock et al., 2021b). Therefore, these data demonstrate
432 that the fine-tuned Drp1 repression, which primes cells for transformation, enriches a
433 subpopulation of cells maintaining more number of smaller fused mitochondrial

434 elements, distinct mitochondrial puncta and minimal mitochondrial content (Extended
435 Fig. 3D). We conclude that the remnant Drp1 driven mitochondrial fission in the weaker
436 Drp1 knockdown population prevents the net fusion of the smaller fused elements to
437 form a larger hyperfused mitochondrial network, and may also underlie generation of
438 the mitochondrial puncta. We speculate that the functional significance of such
439 previously unappreciated distinctions in mitochondrial shape may involve Drp1 driven
440 regulation of mitophagy (Twig & Shirihai, 2011).

441 To probe the contribution of gene expression of any particular cell population in
442 neoplastic transformation after Drp1 repression, we performed sc-RNAseq of the control
443 and Drp1 knockdown Parental populations. First, we compared the overall gene
444 expression within the gene coverage in our scRNA-seq data set. Indeed, the weaker
445 Drp1 knockdown, which maintains higher Drp1 transcript levels, modulates a smaller
446 gene set to a smaller degree compared to the stronger Drp1 knockdown that maintains
447 lower Drp1 transcript levels (Extended. Fig. 4A, B). However, graded Drp1 knockdown
448 has both 'similar' (graded upregulation or downregulation) and 'opposite' effects
449 (upregulation in one and downregulation in the other) (Extended Fig. 4C). The opposite
450 effect is dominated by Krt15, Krt13, Krt4, Krt5 transcripts being upregulated in the
451 weaker Drp1 knockdown and downregulated in the stronger Drp1 knockdown (color
452 coded * in Fig. 4D, Extended Fig. 4C), corroborating our findings on Krt15 protein levels
453 (Fig. 3E). On the other hand, genes for various mitochondrial proteins, involved in
454 mitochondrial energetics, redox or biogenesis, were upregulated particularly in the
455 stronger Drp1 knockdown (Fig. 4E upper panel, Extended Fig. 4C, bold). This is
456 consistent with our observation of decreased mitochondrial content in the weaker Drp1
457 knockdown (Fig. 4B). Synthesis of the mitochondrial proteins can be potentially
458 sustained by elevated ribosomal genes and genes involved in protein synthesis in the
459 stronger Drp1 knockdown (Fig. 4E, lower panel). Although Drp1 repression has been
460 linked with regulation of ribosomal genes and protein synthesis (Tanwar et al.,
461 2016)(Zhao Q et al., 2021)(Favaro, Romanello et al., 2019), this area warrants further
462 focused investigation.

463 Next, we performed cell clustering in a UMAP plot and obtained 6 clusters
464 (Extended. Fig. 4D, Extended Data Table 3). Based on the remarkable correspondence

465 of the top conserved cluster markers identified in the Parental/transformed data set
466 (Fig.2), we assigned cluster identities of G2-M, S-early, S-late, mtDNA-lo, SloCycl-
467 Krt15-hi and Cytokine to the control and Drp1 knockdown data set (Extended. Fig. 4D).
468 The number of common cluster markers show overall 40-80% correspondence between
469 the two data sets, with some exceptions in the S-late and mtDNA-lo clusters (Extended.
470 Fig. 4E). Strikingly, the weaker Drp1-knockdown population exhibits expansion of the
471 SloCycl-Krt15-hi cluster and reduction of the Cytokine and mtDNA-lo clusters observed
472 in the [Drp1^{att}-CyclinE^{hi}-Sox2^{hi}-Krt15^{hi}] TF-1 population, albeit to a lesser degree (Fig.
473 4F). This similarity in cluster organization suggests that the non-transformed Parental
474 population with fine-tuned Drp1 repression establishes a gene expression profile to
475 poise the cells for neoplastic transformation, and thus explains their accelerated
476 neoplastic transformation ability only with higher TCCD dose (Fig. 3L). On the other
477 hand, the stronger Drp1 knockdown markedly reduced the abundance of the SloCycl-
478 Krt15-hi cluster and exhibits overall opposite trend of cluster profile compared to the
479 weaker Drp1 knockdown and TF-1 population (Fig. 4F). Krt15 and various other marker
480 Keratin genes are dramatically suppressed across the clusters in the stronger Drp1
481 knockdown and while they are over all elevated in the weaker Drp1 knockdown
482 (Extended Fig. 4F). This data, suggesting that impact of the level of Drp1 repression on
483 specific keratin transcripts is direct and not due to cluster organization, confirms and
484 expands our findings on Krt15 protein levels (Fig. 3E). Moreover, analyses of cell cycle
485 distribution (as in Fig. 2) revealed higher G2-M score and less S score in the stronger
486 Drp1 knockdown, while weaker Drp1 knockdown has similar cell cycle distribution to the
487 control (Fig. 4G). The stronger Drp1 knockdown maintains more cells in G2-M and less
488 cells in S particularly in the SloCycl-Krt15-hi as well as the mt-DNA-lo cluster (Extended.
489 Fig. 4H), contradictory to their reciprocal nature in the TF-1 population (Fig. 2). The
490 dramatic reduction of the SloCycl-Krt15-hi cluster in the stronger Drp1 knockdown cells
491 could be due to their inability of exiting the elevated CyclinB1/CDK1 driven G2-M
492 regulation in this cluster (Fig. 4H, left). Also, the stronger Drp1 knockdown maintained
493 marked elevation of the growth factor cyclin, Cyclin D2 and reduction of the S phase
494 marker, PCNA, across clusters (Fig. 4H, right); Cyclin E1 and Sox2 transcripts were not
495 detected in this data set. Therefore, our data shows that fine-tuned repression of Drp1,

496 which accelerates carcinogen induced cell transformation, maintains a gene expression
497 profile characteristic of the [Drp1^{att}-CyclinE^{hi}-Sox2^{hi}-Krt15^{hi}] TF-1 population. The
498 stronger Drp1 knockdown fails to do so, has cell cycle disturbances and dramatically
499 reduced expression of relevant keratin genes. We speculate that repression of Drp1
500 beyond an optimal level may initiate compensatory changes through the retrograde
501 pathway to trigger mitochondrial biogenesis and suppress relevant keratin genes (Ryan
502 & Hoogenraad, 2007).
503 Taken together, our detailed molecular analyses of the *in vitro* keratinocyte
504 model suggest that a "goldilocks" level of fine-tuned repression of Drp1 accelerates
505 neoplastic transformation by priming a distinct stem/progenitor-like state (Fig. 5). We
506 propose that the priming is brought about by flexibility of Drp1 regulation that sustains
507 distinct mitochondrial and gene expression characteristics leading to the enrichment of
508 a slow cycling [Drp1^{ftr}-CyclinE^{hi}-Sox2^{hi}-Krt15^{hi}] stem/progenitor-like state. Cyclin E,
509 which maintains expression of stem cell markers, is indispensable for exiting cell cycle
510 quiescence and also for neoplastic transformation (Hwang & Clurman, 2005, Schaefer
511 & Lengerke, 2020, Teixeira & Reed, 2017) (Liu et al., 2019). We speculate that the slow
512 cycling [Drp1^{ftr}-CyclinE^{hi}-Sox2^{hi}-Krt15^{hi}] stem/progenitor-like state has reduced depth of
513 cell cycle quiescence (van Velthoven & Rando, 2019) towards rapidly transitioning to a
514 self-renewing/proliferation state to support neoplastic transformation. Such transition
515 may involve further activation of mitochondrial fission induced by signaling pathways
516 supporting stemness, which would be prevented with supra-optimal Drp1 knockdown
517 (as shown here) or total ablation of Drp1 (as reported) (Kashatus, Nascimento et al.,
518 2015, Serasinghe et al., 2015, Spurlock et al., 2019). This conceptualization helps
519 explain how regulated reduction and increase of Drp1 activity can potentially maintain
520 adult stem cell properties (Iwata et al., 2020, Khacho & Slack, 2017, Parker et al., 2015,
521 Xie et al., 2015). Furthermore, our data raises the possibility that the [Drp1^{att}-CyclinE^{hi}-
522 Sox2^{hi}-Krt15^{hi}] TF-1 population represents an early stage of neoplastic transformation
523 when stem cells self-renew to form less differentiated tumors, unlike the differentiated
524 tumors formed by the [Drp1^{hi}-CyclinE^{lo}-Sox2^{lo}-Krt15^{hi}] TF-10 population. Further *in vivo*
525 validation of our findings would reveal if and how bodily stresses causing mild
526 repression of Drp1 driven mitochondrial fission, can possibly enrich the mitochondria

527 primed stem/progenitor-like population in tissues making them susceptible to neoplastic
528 transformation. Enhanced mitochondrial fusion, proposed as a required event of
529 neoplastic transformation of stem cells (Bonnay et al., 2020), may also involve such
530 mitochondria driven priming.
531

532 **MATERIALS AND METHODS**

533 **Materials**

534 Biochemicals were obtained from Fisher Biochemicals or Sigma. Other materials: Drp1
535 shRNA (Dharmacon); Flouromount G (SouthernBiotech); FuGENE® 6 Transfection
536 Reagent (Promega); Luminata Forte Western HRP substrate (Millipore); 4%
537 paraformaldehyde aqueous solution and Triton X-100 (FisherScientific); Labtek
538 chambers (Nalgene Nunc International); DMEM (GIBCO); Geltrex (GIBCO); Primary
539 antibodies were against: Drp1 (western blotting, 1:1000; immunofluorescence, 1:100;
540 BD Biosciences); Cyclin E1 (HE12) (western blotting, 1:1000; immunofluorescence
541 1:100; Cell Signaling); actin AB-5 (1:10000; BD Biociences), Sox2 (western blotting,
542 1:500; immunofluorescence, 1:100; BD Bioscience), HSP-60 (1:200; BD Bioscience);
543 Cytokeratin 15 (western blotting, 1:2000; immunofluorescence, 1:200; Abcam); Oct4
544 (immunofluorescence, 1:50; Cell Signaling); Nanog (immunofluorescence, 1:50; Cell
545 Signaling). Secondary antibodies were from Jackson ImmunoResearch Laboratories.
546 Athymic nude mice were purchased from Jackson laboratories.

547 **Cell culture methods**

548 HaCaT cells were cultured on plastic dishes in Dulbecco's Modified Eagle's Medium
549 (DMEM) with high glucose (4.5 g/L), sodium pyruvate (1 mM), L-Glutamine (4 mM),
550 Penicillin (100 U/mL), Streptomycin (100 µg/mL), and 10% FBS using standard
551 techniques. Transformed keratinocytes were derived from the Parental HaCaTs by
552 selecting multiple clones after treatment with the noted dose of TCDD with
553 replenishment with fresh TCDD every 2-3 days. The derived lines were treated with two
554 courses of BM-Cyclin treatment to eliminate any mycoplasma infection.

555 Transfections were preformed using Fugene 6 Transfection Reagent modifying
556 manufacturer's protocols. Lines stably expressing Drp1-shRNAs or PSmO were
557 selected using puromycin treatment (2 µg/mL) with regular media changes for 2 weeks
558 until resistant colonies grew. The stable Drp1 knockdown lines were treated with two
559 courses of BM-Cyclin treatment to eliminate any mycoplasma infection.
560 Standard cell proliferation assay was performed as described in (Parker et al.,
561 2015). The extreme limiting dilution analysis (ELDA) of spheroid formation ability was
562 performed by seeding 1, 10, 100, and 1000 cells per well with 24 wells per dose in a 96
563 well UltraLow Attachment plate and TIC-supporting media (DMEM:F12 supplemented
564 with human growth factors as published elsewhere (Spurlock et al., 2019)). Wells were
565 Extendedemented with media equaling 10% of the total volume every second day. On
566 Day 5, the total number of wells for each dose containing nascent spheroids was
567 tabulated. The online ELDA tool was used to analyze the results (Hu & Smyth, 2009).

568 **Immunoblotting and Immunofluorescence**

569 Immunoblotting was performed using standard techniques. Whole cell lysates were run
570 on 10% polyacrylamide gels and transferred to PVDF membranes followed by probing
571 with appropriate primary and secondary antibodies.
572 Immunofluorecence was performed as described previously (Parker et al., 2015)
573 on cells seeded in LabTek 8-well glass bottom or slide chambers. Briefly, cells were
574 fixed in freshly prepared 4% aqueous paraformaldehyde supplemented with 4 %w/v
575 sucrose and permeablized in freshly prepared 0.1 % Triton X-100 prior to staining.
576 Immunostained cells were mounted in Fluoromount with DNA stain Hoechst 33342 (10
577 µg/mL).

578 **Confocal microscopy, image processing and analysis**

579 Confocal microscopy was performed on a Zeiss LSM700 microscope equipped with 405
580 nm, 488 nm, 555 nm, and 639 nm lasers, using the proprietary Zen Black (2012)
581 software. Confocal micrographs were acquired with optimized laser powers and
582 appropriate filters to minimize crosstalk, cross-excitation and bleaching. Live cells were
583 imaged using a temperature and CO_2 controlled chamber set to 37 C and 5% CO_2.

584 Image processing and analysis of relative protein abundance and localization
585 were performed using Zen Black and Zen Blue software to obtain background corrected
586 mean fluorescence intensities within defined regions of interest drawn on maximum
587 intensity z-projections of optical slices. Nuclear and cytosolic regions were demarcated
588 based on DNA stain Hoechst 33342 and the immunostain of the molecule of interest,
589 respectively. The [Fission] and [Fusion1/5] metrics using MitoGraph v2.1 software run
590 on 3D stacks of confocal optical slices acquired from live cells expressing mito-PSmO
591 or stained with Mitotracker Green, as described in (Spurlock et al., 2019). [Fission] is
592 total mitochondria number / total mitochondrial length; [Fusion5] is (sum of top 5
593 mitochondrial length / total mitochondrial length) X 100. Microsoft Excel and IBM SPSS
594 Statistics 23 were used to perform background corrections, bivariate analyses and
595 significance testing.

596 **Tumor Forming Assay in mice and histochemistry**

597 5 million transformed HaCaT cells were injected in subcutaneously in the flank of
598 athymic nude mice to form xenograft tumors. Prior to injection, cells were trypsinized
599 and washed once with sterile PBS, and finally resuspended to 25,000 cells/μL in room
600 temperature PBS with Geltrex. Tumors arising within 6 to 8 months were harvested for
601 histochemical analyses. The harvested tumors were frozen unfixed in TissueTek OCT
602 compound on dry-ice. A Cryostat was used to obtain 5 μm slices, which were then fixed
603 using freshly made cold 4% paraformaldehyde and then stained with H&E using
604 standard techniques.

605 **Single Cell RNAseq and data analyses**

606 Trypsinized single cells were washed in PBS (without ca++ or Mg++) with 0.04% BSA
607 and tested for >90% viability. Single cell analysis was performed on a 10xGenomics
608 platform according to 3' v3.1 NextGem Dual Index manual. The 3'-biased cDNA libraries
609 were constructed through the following steps: cDNA fragmentation, end repair & A-
610 tailing, and size selection by SPRIselect beads, adaptor ligation, and sample index PCR
611 amplification, and then SPRIselect beads size selection again. The final constructed 3'-
612 biased single cell libraries were sequenced by Illumina Nextseq500 machine, targeting

613 total reads per cell for 20,000 at minimum, and the sequencing cycles consisted of 28bp
614 for read 1, 90 bp for read 2, and 10 bp for i7 index, and 10bp for i5 index.
615 Count matrices were generated from the single-cell raw fastq files using 10x
616 genomics *cellranger* software (v.4.0) using hg38 reference genome provided by 10x
617 Genomics. We filtered the data to only include cells expressing at least 2000 detectable
618 genes (using "nFeature_RNA" filter); this also filtered out dead cells with >10% mt-DNA
619 gene expression in our data set. Our data coverage included approximately ~ 3000
620 genes in average of 5000 cells in each population. The resulting count matrices were
621 analyzed by Seurat package (v3.9.9) with the standard workflow (Butler *et al*, 2018;
622 Stuart *et al*, 2019). After applying the (*nFeature_RNA* > 2000), the expression data were
623 then normalized using the *NormalizeData* function in Seurat and variable featuresets
624 were identified using the *FindVariableFeatures* function in Seurat. Depending on the
625 type of comparison, specific sets of samples were combined using the *IntegrateData*
626 function. The integrated datasets were scaled and cells were clustered with up to 20
627 dimensions (dim=1:20). We performed clustering using several resolution parameters
628 (0.1-0.8) and visually selected optimal resolution for specific datasets. The clusters were
629 visualized using UMAP with up to 20 dimensions. Marker genes for each cluster were
630 calculated with the *FindAllMarkers* function and statistical significance was calculated by
631 Wilcoxon Rank Sum test. Differential expression of the cluster markers was carried out
632 using the FindMarkers function of Seurat. For this, we only used the normalized data
633 before integration (assay 'RNA') using the Wilcoxon rank sum test, as suggested by
634 Seurat documentation. For cell-cycle scoring, we use the CellCycleScoring function of
635 Seurat, which provides scores of G2M and S phase scores and assigns cell-cycle
636 phases based on these scores (Tirosh *et al*, 2016). The cell-lineage determination and
637 trajectory calculation were carried out using the *Slingshot* (Street *et al*, 2018) package
638 with Seurat clusters and default parameters. The algorithm was allowed to automatically
639 identify the start and the end clusters. GSEA analyses were performed with ranked log
640 fold change (LFC) of markers (>0.1, p<0.01) using MsigDB as described in (Tanwar et
641 al., 2016). Overrepresentation analyses were performed with genes with negative LFC
642 in Cluster 5 using the Reactome PA package of R v 3.6.0.

643

644 **Statistical analyses:**

645 Drawing of plots and statistical analyses were performed using Excel, SPSS or R
646 package as mentioned in appropriate section above.

647

648 **ACKNOWLEDGEMENTS:**

649 BS, KM, AM are supported by NIH award (# R33ES025662). We acknowledge Dezhi
650 Wang from the Pat Pathology Core Research Laboratory for preparation of H&E stained
651 slides, the UAB Flow Cytometry and Single Cell Services Core that is supported by
652 AR048311, AI027667, and the Dr. Mike Crowley from the Heflin Genomics Core for sc-
653 RNAseq.

654 **AUTHOR CONTRIBUTION**

655 BS designed and performed experiments and analyzed data along with AM and AG; DP
656 generated the transformed lines and performed basic characterization; ABH supervised
657 the xenograft experiments performed by BS and SG; GPS performed the pathological
658 evaluation of tumor sections; SL provided consultation for the sc-RNAseq and prepared
659 the scRNAseq library; MKB provided consultation for the sc-RNAsq analyses and
660 performed the analyses; KM conceived the study, helped in experimental design,
661 analyzed data and wrote the manuscript with BS.

662 **DECLARATION OF INTEREST**

663 The authors declare no competing interests.

664

665

666

667

668

669

670 **FIGURE LEGENDS:**

671 **Figure 1. Keratinocytes transformed under mild carcinogenic stress exhibit**
672 **attenuated Drp1 activity and have abundant self-renewing/proliferating cells.**
673 **A)** Cell proliferation assay (quantified by crystal violet staining) of HaCaT cells after
674 exposure to TCDD (1 or 10 nM) over 4 and 16 days, with Toluene (10nM) as vehicle
675 control. **B)** Immunoblot analyses of AHR and actin (loading control) in transformed
676 HaCaT populations, TF-1 and TF-10, in the absence of TCDD. **C)** Representative
677 micrographs (40X) of H&E stained sections of tumor xenografts formed by TF-1 and TF-
678 10 HaCaT cells; zoom of boxed region shown in the bottom panels. **D)** Immunoblot
679 analyses of Drp1, pDrp1(S616), Mfn1, Mfn2, Opa1 and actin (loading control) in TF-1
680 and TF-10 HaCaT cells. **E)** Maximum intensity projection of confocal optical sections of
681 representative Parental, TF-1 and TF-10 HaCaT cells expressing mitoPSmO. **F)**
682 Quantification of mitochondrial [Fission] and [Fusion5] metrics from micrographs
683 represented in (E). **G)** Quantification of cell proliferation assay (as in A) of Parental, TF-
684 1 and TF-10 HaCaT cells over 7 days in the absence of TCDD. **H)** Representative
685 micrograph showing spheroids formed when 10^4 Parental, TF-1 or TF-10 HaCaT cells
686 were maintained in low attachment plate in presence of stem cell medium. **I)**
687 Quantification of spheroid forming frequency of Parental, TF-1 or TF-10 HaCaT cells
688 using ELDA. * signifies p value of <0.05 in T test (A,F) and ELDA (I); scale bar depicts
689 10 μm (D) and 100 μm (H).
690

691 **Figure. 2. Drp1 attenuated TF-1 keratinocyte population maintains an expanded**
692 **slow-cycling subpopulation with elevated stem/progenitor cell markers**. **A)** UMAP
693 plot of scRNA-seq derived clusters (0-5) of Parental, TF-1 and TF-10 HaCaT cells (top);
694 pie chart of the percentage distribution of the clusters (bottom, p value from ChiSquare
695 test); color coded arrows point the clusters with unique reciprocal abundance in TF-1
696 cells. **B)** Violin plots depicting expression of Krt13, Krt15, Krt5, Sox2 and Sox4 in the
697 clusters identified in (A) in the Parental, TF-1 and TF-10 HaCaT cells; color coded arrow
698 point to Cluster 3 marked by Krts. **C)** Normalized Enrichment Scores (NES) of functional
699 pathways identified by GSEA analyses of marker genes of Clusters 0-4 (Extended data
700 Table 2) and by overrepresentation analyses for Cluster 5 (* represents categories

701 including mtDNA genes); functional categories defined by majority of the leading-edge
702 genes are in parentheses, while clusters are arranged based on trajectory analyses
703 (open arrows) (see Extended Fig. 2F). **D)** Violin plots depicting expression of cyclinA2,
704 cyclinB1, CDK1, cyclinD2 and PCNA in the clusters identified in (A) in the Parental, TF-
705 1 and TF-10 HaCaT cells; the functional category of genes identified in (C) is included in
706 the cluster identity. **E)** Distribution of G2-M and S scores obtained by gene expression
707 analyses of cell cycle predictive genes in the Parental, TF-1 and TF-10 HaCaT cells. **F)**
708 Feature plot of G2-M and S scores obtained from (E). **G)** Bar plot showing fraction of
709 cells in G2-M, S and G0/G1, computed from (E) in the functionally categorized clusters
710 in the Parental, TF-1 and TF-10 HaCaT cells; inset shows G1 to S reciprocity of the
711 clusters (color-coded arrows) with unique reciprocal abundance in TF-1 cells in (A).
712
713 **Figure 3. Fine-tuned repression of Drp1 sustains a [CyclinE^{hi}-Sox2^{hi}-Krt15^{hi}] state**
714 **and accelerates carcinogen driven cell transformation**. **A)** Immunoblot analyses of
715 Sox2, Krt15 and actin (loading control) in Parental and TF-1 and TF-10 HaCaT cells. **B)**
716 Dot plot of [Sox2] and [Krt15] levels obtained from confocal micrographs of co-
717 immunostained Parental and TF-1 HaCaT cells; black lines, marking 4 quadrants,
718 represent levels of Sox2 and Krt15 determined from normalized signal in each
719 population (see Extended Fig. 3B). **C)** Dot plot of [Sox2] and [Drp1] levels obtained from
720 confocal micrographs of co-immunostained Parental and TF-1 HaCaT cells; dotted lines
721 mark the levels of [Drp1] in cells expressing higher [Sox2] levels. **D)** Dot plot of [Sox2]
722 and [pDrp1(S616)] levels obtained from confocal micrographs of co-immunostained
723 Parental and TF-1 HaCaT cells; dotted lines mark the levels of [pDrp1(S616)] in cells
724 expressing higher [Sox2] levels. **E)** Immunoblot analyses of Drp1, Krt15, Sox2 and actin
725 (loading control) in Parental HaCaT cells expressing non-targeted shRNA (Cnt), weaker
726 (W) or stronger (S) Drp1 shRNA. **F)** Immunoblot analyses of Cyclins E1, E2, A2, B1, D2
727 and actin (loading control) in Parental and stable TF-1 and TF-10 HaCaT cells. **G)**
728 Representative confocal micrographs of Cyclin E1 immunostaining in Parental and TF-1
729 HaCaT cells; N depict the nucleus in each cell identified by DNA stain (not shown). **H)**
730 Box plot showing quantification of nuclear to cytosolic ratio of Cyclin E1 levels quantified
731 from experiment described in (G). **I)** Dot plot of [Sox2] and [CyclinE1(pT62)] levels

732 obtained from confocal micrographs of co-immunostained Parental and TF-1 HaCaT
733 cells; dotted lines mark the levels of [CyclinE1(pT62)] in cells expressing higher [Sox2]
734 levels. **J)** Representative images of Cyclin E1 immunostaining in Parental HaCat cells
735 expressing non-targeted shRNA (Cnt), weaker (W) or stronger (S) Drp1 shRNA. **K)** Box
736 plot showing quantification of nuclear to cytosolic ratio of Cyclin E1 levels quantified
737 from experiment described in (J). **L)** Cell proliferation assay of Parental HaCaT cells
738 expressing non-targeted shRNA (Cnt), weaker (W) or stronger (S) Drp1 shRNA after
739 exposure to TCDD (1nM or 10nM) at an early and a late time point in the neoplastic
740 transformation protocol; 'Toluene' is the vehicle control for TCDD and 'Control' is with
741 no chemical. * signifies p value of <0.05 in KW (G) and T test (L); scale bar depicts 20
742 μm.
743
744 **Figure 4. Fine-tuned repression of Drp1 maintains smaller fused mitochondrial**
745 **elements, and sustains transcriptomic profile similar to the neoplastic stem cell**
746 **enriched TF-1 population. A)** Dot plot of [Fission] and [Fusion5] obtained from
747 confocal micrographs of Mitotracker green stained live Parental HaCaT cells expressing
748 non-targeted shRNA as control (Cnt), weaker (W) or stronger (S) Drp1 shRNA; numbers
749 denote the percentage of cells in the adjacent boxes with p value from ChiSquare test;
750 representative images in Extended Fig. 3D **B)** Dot plot of [Fission] or [Fusion5] of single
751 cells (from A) with their total mitochondrial number and total mitochondrial length; lines
752 represent the ranges of [Fission] and [Fusion5] to demarcate cell subpopulations in
753 boxes in (A). **C)** Bar graph signifying percentage of cells from (A) with >80 [Fusion1]
754 metric (top); dot plot of [Fission] and [Fusion1] of cells from (A) (bottom). **D)** Barplots
755 showing positive and negative log fold change values of top 20 genes in Parental
756 HaCaT cells expressing weaker (W) (Top) or stronger (S) (bottom) shRNA with respect
757 to the cells expressing non-targeting shRNA (Cnt); 0 signifies no change and color
758 coded * denote relevant Krt genes. **E)** Barplot showing ratio of absolute expression
759 values of mitochondrial genes (top) and ribosomal or protein translation genes (bottom)
760 in the Parental HaCat cells expressing the stronger (S) or the weaker (W) Drp1 shRNA
761 with respect to those expressing non-targeting shRNA (Cnt); 1 signifies no change. **F)**
762 Line plot showing % population of Parental cells expressing the strong (S) or weak (W)

763 Drp1 shRNA in the named scRNA-seq derived cell clusters, with respect to those
764 expressing non-targeting shRNA (Cnt). This is compared to the same in the TF-1 cells
765 with respect to its Parental population; 1 signifies no change from respective control. **G)**
766 Distribution of G2-M and S scores obtained by gene expression analyses of cell cycle
767 predictive genes in the Parental HaCaT cells expressing non-targeted shRNA (Cnt),
768 weaker Drp1-shRNA (W) or stronger shRNA (S). **H)** Violin plots depicting expression of
769 cyclinB1, CDK1 (left panel) and cyclinD2, PCNA (right panel) in the named scRNA-seq
770 derived cell clusters in the Parental HaCaT cells expressing non-targeted shRNA (Cnt),
771 weaker Drp1-shRNA (W) or stronger shRNA (S).
772
773 **Figure. 5. Proposed model of a 'Goldilocks' zone of Drp1 activity for priming a**
774 **stem/progenitor like state to accelerate neoplastic transformation.** In a
775 keratinocyte model, a level of fine-tuned repression (ftr) of Drp1 maintains smaller fused
776 mitochondrial networks and sustains a state of [Drp1^{ftr}-CyclinE^{hi}-Sox2^{hi}-Krt15^{+}], which is
777 susceptible to carcinogen (TCDD) driven neoplastic transformation. Low dose of TCDD
778 driven transformation leads to a similar Drp1 attenuated (att) state of [Drp1^{att}-CyclinE^{hi}-
779 Sox2^{hi}-Krt15^{+}] that forms less differentiated (primitive) tumors, while a 10-fold higher
780 TCDD dose transforms cells to a state of [Drp1^{hi}-CyclinE^{lo}-Sox2^{lo}-Krt15^{+}] that forms
781 differentiated tumors. Supra optimal repression of Drp1 maintains hyperfused
782 mitochondria and sustains a state of [Drp1^{lo}-CyclinE^{hi}-Sox2^{hi}-Krt15^{-}], which prevents
783 carcinogen driven neoplastic transformation.
784
785
786
787
788
789
790
791
792
793
794

795 **EXTENDED FIGURE LEGENDS:**

796 **Extended Figure 1. A)** Quantification of incidence and volume of xenograft tumors
797 formed by TF-1 and TF-10 HaCaT cells; # indicates presence of a distant tumor. **B)**
798 Immunoblot analyses of Cytochrome C, Fis1, Tom20 and actin (loading control) in
799 Parental and TF-1 and TF-10 HaCaT cells.

800 **Extended Figure 2. A)** Bar plot showing the percentage distribution of the clusters (0-5)
801 in each of the cell populations identified by scRNA-seq analyses of Parental, TF-1 and
802 TF-10 HaCat cells (left); numbers show cell cycle distribution from flowcytometry
803 analyses of PI stained cells in the corresponding population (right). **B)** UMAP plot of
804 scRNA-seq derived clusters (0-5) of Parental, TF-1 and TF-10 HaCaT cells obtained
805 with minimum cluster resolution; color coded arrows point the major change in cluster
806 distribution in transformed cells. **C)** Heat map of statistically significant marker genes for
807 the color-coded clusters (0-5) of Parental, TF-1 and TF-10 HaCaT cells; color coded
808 arrows point to the top most marker gene in the 3 clusters that are have different
809 distribution between the Parental and transformed populations; color index shows log
810 fold change; * marks the Histone gene cluster. **D)** Violin plots depicting expression of
811 the mt-DNA genes in the named scRNA-seq derived cell clusters in the Parental, TF-1
812 and TF-10 HaCaT cells. **E)** Violin plots depicting expression of HES1 and OASL genes
813 in the named scRNA-seq derived cell clusters in the Parental, TF-1 and TF-10 HaCaT
814 cells. **F)** PCA plot of trajectory analyses of the scRNA-seq derived cell clusters in the
815 Parental, TF-1 and TF-10 HaCaT cells.

816 **Extended Figure 3. A)** Representative confocal micrographs of immunostained
817 Parental and TF-1 HaCaT cells showing endogenous expression of Oct4, Nanog and
818 Sox2; blue depicting nuclear staining with Hoechst. **B)** Dot plot of [Sox2] and [Krt15]
819 obtained from confocal micrographs of co-immunostained Parental and TF-1 HaCaT
820 cells; [Sox2] levels normalized to the minimum in the respective population (left) and
821 [Krt15] levels normalized to the minimum in the respective population (right); black lines
822 demarcate levels of Sox2 and Krt15 as determined from the normalized signal of the
823 other. **C)** Representative confocal micrographs of Parental and TF-1 HaCaT cells
824 showing endogenous expression of Tom20 and Cyclin E1 after 2 hours incubation with

825 DMSO or Cychloheximide, with the pre-incubation time point (0h) as control. **D)**
826 Representative maximum intensity projections (MIP) of confocal optical sections
827 (micrograph) and the corresponding MitoGraph generated binary images (binary) for
828 quantifying [Fission] and [Fusion1/5] metrics of the Parental HaCaT cells expressing
829 non-targeted shRNA (Cnt), strong (S) or weak (W) Drp1 shRNA; the cells represent
830 populations in colored boxes in Fig. 4A while the number depicts their abundance in
831 percentage. Scale bar depicts 100 μm (A, C) or 15 μm (D).

832 **Extended Figure 4. A)** Bar plot showing the knockdown efficiency of strong (S) or weak
833 (W) Drp1 shRNA expressed as ratio of Drp1 transcript levels in the knockdown HaCaT
834 and that of the cells expressing the non-targeted shRNA control. **B)** Bar plot showing
835 log fold change of overall gene expression of Parental HaCaT cells expressing strong
836 (S) or weak (W) Drp1 shRNA with respect to those expressing the non-targeted shRNA
837 (Cnt). **C)** Plots showing ratio of the expression of covered genes between the Parental
838 HaCaT cells expressing strong (S) or weak (W) Drp1 shRNA; "Similar effects" showing
839 ratio of increase or decrease in the (S) Drp1 shRNA over the (W) Drp1 shRNA (back
840 arrows in left panel), while opposite effects showing opposite trends in genes as
841 labelled in the arrows (back arrows right panel); grey arrows point to the top 20 genes of
842 each category. **D)** UMAP plot of scRNA-seq based clusters (0-5) of Parental HaCaT
843 cells expressing non-targeted shRNA (Cnt), strong (S) or weak (W) Drp1 shRNA; arrow
844 pointing the SloCyc-Krt15-hi cluster (note color coding is not same as the one presented
845 in Fig. 2). **E)** Bar plot showing percentage of statistically significant common genes
846 (Upregulated or Downregulated) between color coded clusters obtained with the
847 scRNA-seq data set of parental and transformed HaCaT cells (Fig. 2) and that of
848 parental expressing control or Drp1 shRNAs (Fig. 4); same color coding is maintained
849 between the two data sets. **F)** Violin plots depicting expression of Krt13, Krt15, Krt4,
850 Krt5, Krt6A, Krt7 genes in the named scRNA-seq based cell clusters in the Parental
851 HaCaT cells expressing non-targeted shRNA (Cnt), strong (S) or weak (W) Drp1
852 shRNA. **G)** Bar plot showing fraction of cells in G2-M, S and G0/G1, computed from
853 main Fig. 4G, in the functionally categorized clusters in the Parental cells expressing
854 non-targeted shRNA (Cnt), strong (S) or weak (W) Drp1 shRNA.
855

856 **REFERENCES**

857

858 Boelsma E, Verhoeven MC, Ponec M (1999) Reconstruction of a human skin equivalent
859 using a spontaneously transformed keratinocyte cell line (HaCaT). J Invest Dermatol
860 112: 489-98
861
862 Bonnay F, Veloso A, Steinmann V, Kocher T, Abdusselamoglu MD, Bajaj S, Rivelles E,
863 Landskron L, Esterbauer H, Zinzen RP, Knoblich JA (2020) Oxidative Metabolism
864 Drives Immortalization of Neural Stem Cells during Tumorigenesis. Cell 182: 1490-1507
865 e19
866
867 Boumahdi S, Driessens G, Lapouge G, Rorive S, Nassar D, Le Mercier M, Delatte B,
868 Caauwe A, Lenglez S, Nkusi E, Brohee S, Salmon I, Dubois C, del Marmol V, Fuks F,
869 Beck B, Blanpain C (2014) SOX2 controls tumour initiation and cancer stem-cell
870 functions in squamous-cell carcinoma. Nature 511: 246-50
871
872 Butler A, Hoffman P, Smibert P, Papalexi E & Satija R (2018) Integrating single-cell
873 transcriptomic data across different conditions, technologies, and species. *Nature*
874 *Biotechnology* 36: 411–420
875
876 Chen H, Chan DC (2017) Mitochondrial Dynamics in Regulating the Unique Phenotypes
877 of Cancer and Stem Cells. Cell Metab 26: 39-48
878
879 Der Vartanian A, Quetin M, Michineau S, Aurade F, Hayashi S, Dubois C, Rocancourt
880 D, Drayton-Libotte B, Szegedi A, Buckingham M, Conway SJ, Gervais M, Relaix F
881 (2019) PAX3 Confers Functional Heterogeneity in Skeletal Muscle Stem Cell
882 Responses to Environmental Stress. Cell Stem Cell 24: 958-973 e9
883
884 Di Meglio P, Duarte JH, Ahlfors H, Owens ND, Li Y, Villanova F, Tosi I, Hirota K, Nestle
885 FO, Mrowietz U, Gilchrist MJ, Stockinger B (2014) Activation of the aryl hydrocarbon
886 receptor dampens the severity of inflammatory skin conditions. Immunity 40: 989-1001
887
888 Favaro G, Romanello V, Varanita T, Andrea Desbats M, Morbidoni V, Tezze C, Albiero
889 M, Canato M, Gherardi G, De Stefani D, Mammucari C, Blaauw B, Boncompagni S,
890 Protasi F, Reggiani C, Scorrano L, Salviati L, Sandri M (2019) DRP1-mediated
891 mitochondrial shape controls calcium homeostasis and muscle mass. Nat Commun 10:
892 2576
893
894 Folmes CD, Dzeja PP, Nelson TJ, Terzic A (2012) Metabolic plasticity in stem cell
895 homeostasis and differentiation. Cell Stem Cell 11: 596-606
896
897 Foronda M, Martinez P, Schoeftner S, Gomez-Lopez G, Schneider R, Flores JM,
898 Pisano DG, Blasco MA (2014) Sox4 links tumor suppression to accelerated aging in
899 mice by modulating stem cell activation. Cell Rep 8: 487-500
900
901 Friedman JR, Nunnari J (2014) Mitochondrial form and function. Nature 505: 335-43

Fuchs E (2016) Epithelial Skin Biology: Three Decades of Developmental Biology, a Hundred Questions Answered and a Thousand New Ones to Address. Curr Top Dev Biol 116: 357-74

Geng Y, Yu Q, Sicinska E, Das M, Schneider JE, Bhattacharya S, Rideout WM, Bronson RT, Gardner H, Sicinski P (2003) Cyclin E ablation in the mouse. Cell 114: 431-43

Giroux V, Lento AA, Islam M, Pitarresi JR, Kharbanda A, Hamilton KE, Whelan KA, Long A, Rhoades B, Tang Q, Nakagawa H, Lengner CJ, Bass AJ, Wileyto EP, Klein-Szanto AJ, Wang TC, Rustgi AK (2017) Long-lived keratin 15+ esophageal progenitor cells contribute to homeostasis and regeneration. J Clin Invest 127: 2378-2391

Gonzales KAU, Fuchs E (2017) Skin and Its Regenerative Powers: An Alliance between Stem Cells and Their Niche. Dev Cell 43: 387-401

Hao N, Lee KL, Furness SG, Bosdotter C, Poellinger L, Whitelaw ML (2012) Xenobiotics and loss of cell adhesion drive distinct transcriptional outcomes by aryl hydrocarbon receptor signaling. Mol Pharmacol 82: 1082-93

Hoppins S (2014) The regulation of mitochondrial dynamics. Curr Opin Cell Biol 29: 46-52

Hu Y, Smyth GK (2009) ELDA: extreme limiting dilution analysis for comparing depleted and enriched populations in stem cell and other assays. J Immunol Methods 347: 70-8

Hwang HC, Clurman BE (2005) Cyclin E in normal and neoplastic cell cycles. Oncogene 24: 2776-86

Iwata R, Casimir P, Vanderhaeghen P (2020) Mitochondrial dynamics in postmitotic cells regulate neurogenesis. Science 369: 858-862

Jung MH, Jung SM, Shin HS (2016) Co-stimulation of HaCaT keratinization with mechanical stress and air-exposure using a novel 3D culture device. Sci Rep 6: 33889

Kageyama Y, Zhang Z, Sesaki H (2011) Mitochondrial division: molecular machinery and physiological functions. Curr Opin Cell Biol 23: 427-34

Karantza V (2011) Keratins in health and cancer: more than mere epithelial cell markers. Oncogene 30: 127-38

Kashatus JA, Nascimento A, Myers LJ, Sher A, Byrne FL, Hoehn KL, Counter CM, Kashatus DF (2015) Erk2 phosphorylation of Drp1 promotes mitochondrial fission and MAPK-driven tumor growth. Mol Cell 57: 537-51

Khacho M, Clark A, Svoboda DS, Azzi J, MacLaurin JG, Meghaizel C, Sesaki H, Lagace DC, Germain M, Harper ME, Park DS, Slack RS (2016) Mitochondrial Dynamics Impacts Stem Cell Identity and Fate Decisions by Regulating a Nuclear Transcriptional Program. Cell Stem Cell 19: 232-247

Khacho M, Slack RS (2017) Mitochondrial activity in the regulation of stem cell self-renewal and differentiation. Curr Opin Cell Biol 49: 1-8

Leclerc D, Staats Pires AC, Guillemin GJ, Gilot D (2021) Detrimental activation of AhR pathway in cancer: an overview of therapeutic strategies. Curr Opin Immunol 70: 15-26

Li S, Park H, Trempus CS, Gordon D, Liu Y, Cotsarelis G, Morris RJ (2013) A keratin 15 containing stem cell population from the hair follicle contributes to squamous papilloma development in the mouse. Mol Carcinog 52: 751-9

Liang R, Arif T, Kalmykova S, Kasianov A, Lin M, Menon V, Qiu J, Bernitz JM, Moore K, Lin F, Benson DL, Tzavaras N, Mahajan M, Papatsenko D, Ghaffari S (2020) Restraining Lysosomal Activity Preserves Hematopoietic Stem Cell Quiescence and Potency. Cell Stem Cell 26: 359-376 e7

Lisowski P, Kannan P, Mlody B, Prigione A (2018) Mitochondria and the dynamic control of stem cell homeostasis. EMBO Rep 19

Liu L, Michowski W, Kolodziejczyk A, Sicinski P (2019) The cell cycle in stem cell proliferation, pluripotency and differentiation. Nat Cell Biol 21: 1060-1067

Luecken MD, Theis FJ (2019) Current best practices in single-cell RNA-seq analysis: a tutorial. Mol Syst Biol 15: e8746

Maga G, Hubscher U (2003) Proliferating cell nuclear antigen (PCNA): a dancer with many partners. J Cell Sci 116: 3051-60

Magee JA, Piskounova E, Morrison SJ (2012) Cancer stem cells: impact, heterogeneity, and uncertainty. Cancer Cell 21: 283-96

Mandal S, Freije WA, Guptan P, Banerjee U (2010) Metabolic control of G1-S transition: cyclin E degradation by p53-induced activation of the ubiquitin-proteasome system. J Cell Biol 188: 473-9

Mitra K, Lippincott-Schwartz J (2010) Analysis of mitochondrial dynamics and functions using imaging approaches. Curr Protoc Cell Biol Chapter 4: Unit 4 25 1-21

Mitra K, Rikhy R, Lilly M, Lippincott-Schwartz J (2012) DRP1-dependent mitochondrial fission initiates follicle cell differentiation during Drosophila oogenesis. J Cell Biol 197: 487-97

Mitra K, Wunder C, Roysam B, Lin G, Lippincott-Schwartz J (2009) A hyperfused mitochondrial state achieved at G1-S regulates cyclin E buildup and entry into S phase. Proc Natl Acad Sci U S A 106: 11960-5

Moriyama M, Durham AD, Moriyama H, Hasegawa K, Nishikawa S, Radtke F, Osawa M (2008) Multiple roles of Notch signaling in the regulation of epidermal development. Dev Cell 14: 594-604

Morris RJ, Liu Y, Marles L, Yang Z, Trempus C, Li S, Lin JS, Sawicki JA, Cotsarelis G (2004) Capturing and profiling adult hair follicle stem cells. Nat Biotechnol 22: 411-7

Mulero-Navarro S, Fernandez-Salguero PM (2016) New Trends in Aryl Hydrocarbon Receptor Biology. Front Cell Dev Biol 4: 45

Nagdas S, Kashatus JA, Nascimento A, Hussain SS, Trainor RE, Pollock SR, Adair SJ, Michaels AD, Sesaki H, Stelow EB, Bauer TW, Kashatus DF (2019) Drp1 Promotes KRas-Driven Metabolic Changes to Drive Pancreatic Tumor Growth. Cell Rep 28: 1845-1859 e5

Orford KW, Scadden DT (2008) Deconstructing stem cell self-renewal: genetic insights into cell-cycle regulation. Nat Rev Genet 9: 115-28

Otsuki L, Brand AH (2018) Cell cycle heterogeneity directs the timing of neural stem cell activation from quiescence. Science 360: 99-102

Parker DJ, Iyer A, Shah S, Moran A, Hjelmeland AB, Basu MK, Liu R, Mitra K (2015) A new mitochondrial pool of cyclin E, regulated by Drp1, is linked to cell-density-dependent cell proliferation. J Cell Sci 128: 4171-82

Pauklin S, Vallier L (2013) The cell-cycle state of stem cells determines cell fate propensity. Cell 155: 135-47

Prieto J, Leon M, Ponsoda X, Sendra R, Bort R, Ferrer-Lorente R, Raya A, Lopez-Garcia C, Torres J (2016) Early ERK1/2 activation promotes DRP1-dependent mitochondrial fission necessary for cell reprogramming. Nat Commun 7: 11124

Purba TS, Haslam IS, Poblet E, Jimenez F, Gandarillas A, Izeta A, Paus R (2014) Human epithelial hair follicle stem cells and their progeny: current state of knowledge, the widening gap in translational research and future challenges. Bioessays 36: 513-25

Ray SS, Swanson HI (2004) Dioxin-induced immortalization of normal human keratinocytes and silencing of p53 and p16INK4a. J Biol Chem 279: 27187-93

Ryan MT, Hoogenraad NJ (2007) Mitochondrial-nuclear communications. Annu Rev Biochem 76: 701-22

1040 Sang L, Coller HA, Roberts JM (2008) Control of the reversibility of cellular quiescence
1041 by the transcriptional repressor HES1. Science 321: 1095-100
1042
1043 Schaefer T, Lengerke C (2020) SOX2 protein biochemistry in stemness,
1044 reprogramming, and cancer: the PI3K/AKT/SOX2 axis and beyond. Oncogene 39: 278-
1045 292
1046
1047 Schoop VM, Mirancea N, Fusenig NE (1999) Epidermal organization and differentiation
1048 of HaCaT keratinocytes in organotypic coculture with human dermal fibroblasts. J Invest
1049 Dermatol 112: 343-53
1050
1051 Schrepfer E, Scorrano L (2016) Mitofusins, from Mitochondria to Metabolism. Mol Cell
1052 61: 683-694
1053
1054 Senos Demarco R, Uyemura BS, D'Alterio C, Jones DL (2019) Mitochondrial fusion
1055 regulates lipid homeostasis and stem cell maintenance in the Drosophila testis. Nat Cell
1056 Biol 21: 710-720
1057
1058 Serasinghe MN, Wieder SY, Renault TT, Elkholi R, Asciolla JJ, Yao JL, Jabado O,
1059 Hoehn K, Kageyama Y, Sesaki H, Chipuk JE (2015) Mitochondrial division is requisite
1060 to RAS-induced transformation and targeted by oncogenic MAPK pathway inhibitors.
1061 Mol Cell 57: 521-36
1062
1063 Seykora JT, Cotsarelis G (2011) Keratin 15-positive stem cells give rise to basal cell
1064 carcinomas in irradiated Ptch1(+/-) mice. Cancer Cell 19: 5-6
1065
1066 Siegle JM, Basin A, Sastre-Perona A, Yonekubo Y, Brown J, Sennett R, Rendl M,
1067 Tsirigos A, Carucci JA, Schober M (2014) SOX2 is a cancer-specific regulator of tumour
1068 initiating potential in cutaneous squamous cell carcinoma. Nat Commun 5: 4511
1069
1070 Simpson CL, Tokito MK, Uppala R, Sarkar MK, Gudjonsson JE, Holzbaur ELF (2021)
1071 NIX initiates mitochondrial fragmentation via DRP1 to drive epidermal differentiation.
1072 Cell Rep 34: 108689
1073
1074 Siu KT, Rosner MR, Minella AC (2012) An integrated view of cyclin E function and
1075 regulation. Cell Cycle 11: 57-64
1076
1077 Spurlock B, Gupta P, Basu MK, Mukherjee A, Hjelmeland AB, Darley-Usmar V, Parker
1078 D, Foxall ME, Mitra K (2019) New quantitative approach reveals heterogeneity in
1079 mitochondrial structure-function relations in tumor initiating cells. J Cell Sci
1080
1081 Spurlock B, Tullet J, Hartman JLt, Mitra K (2020) Interplay of mitochondrial fission-
1082 fusion with cell cycle regulation: Possible impacts on stem cell and organismal aging.
1083 Exp Gerontol 135: 110919
1084

1085 Spurlock B and Mitra K (2021a) Methods Molecular Biology, Vol. 2275, Volkmar
1086 Weissig and Marvin Edeas (Eds): Mitochondrial Medicine , 978-1-0716-1261-3,
1087 482923_2_En, (Chapter 27).
1088
1089 Spurlock B, Hanumanthu VS and Mitra K (2021b). Strategy of Isolating 'Primed' Tumor
1090 Initiating Cells Based on Mitochondrial Transmembrane Potential. Bio-protocol online,
1091 inPress.
1092
1093 St John LS, Sauter ER, Herlyn M, Litwin S, Adler-Storthz K (2000) Endogenous p53
1094 gene status predicts the response of human squamous cell carcinomas to wild-type
1095 p53. Cancer Gene Ther 7: 749-56
1096
1097 Street K, Risso D, Fletcher RB, Das D, Ngai J, Yosef N, Purdom E & Dudoit S (2018)
1098 Slingshot: cell lineage and pseudotime inference for single-cell transcriptomics. *BMC*
1099 *Genomics* 19: 477
1100
1101 Stuart T, Butler A, Hoffman P, Hafemeister C, Papalexi E, Mauck WM, Hao Y,
1102 Stoeckius M, Smibert P & Satija R (2019) Comprehensive Integration of Single-Cell
1103 Data. *Cell* 177: 1888-1902.e21
1104
1105 Subramanian A, Tamayo P, Mootha VK, Mukherjee S, Ebert BL, Gillette MA, Paulovich
1106 A, Pomeroy SL, Golub TR, Lander ES, Mesirov JP (2005) Gene set enrichment
1107 analysis: a knowledge-based approach for interpreting genome-wide expression
1108 profiles. Proc Natl Acad Sci U S A 102: 15545-50
1109
1110 Tirosh I, Izar B, Prakadan SM, Wadsworth MH, Treacy D, Trombetta JJ, Rotem A,
1111 Rodman C, Lian C, Murphy G, *et al* (2016) Dissecting the multicellular ecosystem of
1112 metastatic melanoma by single-cell RNA-seq. *Science* 352: 189–196
1113
1114 Tanwar DK, Parker DJ, Gupta P, Spurlock B, Alvarez RD, Basu MK, Mitra K (2016)
1115 Crosstalk between the mitochondrial fission protein, Drp1, and the cell cycle is identified
1116 across various cancer types and can impact survival of epithelial ovarian cancer
1117 patients. Oncotarget 7: 60021-60037
1118
1119 Teixeira LK, Reed SI (2017) Cyclin E Deregulation and Genomic Instability. Adv Exp
1120 Med Biol 1042: 527-547
1121
1122 Tsuyoshi H, Orisaka M, Fujita Y, Asare-Werehene M, Tsang BK, Yoshida Y (2020)
1123 Prognostic impact of Dynamin related protein 1 (Drp1) in epithelial ovarian cancer. BMC
1124 Cancer 20: 467
1125
1126 van Velthoven CTJ, Rando TA (2019) Stem Cell Quiescence: Dynamism, Restraint, and
1127 Cellular Idling. Cell Stem Cell 24: 213-225
1128
1129 Twig G, Shirihai OS (2011) The interplay between mitochondrial dynamics and
1130 mitophagy. Antioxid Redox Signal 14: 1939-51

Vantaggiato C, Castelli M, Giovarelli M, Orso G, Bassi MT, Clementi E, De Palma C (2019) The Fine Tuning of Drp1-Dependent Mitochondrial Remodeling and Autophagy Controls Neuronal Differentiation. Front Cell Neurosci 13: 120

Wincent E, Bengtsson J, Mohammadi Bardbori A, Alsberg T, Luecke S, Rannug U, Rannug A (2012) Inhibition of cytochrome P4501-dependent clearance of the endogenous agonist FICZ as a mechanism for activation of the aryl hydrocarbon receptor. Proc Natl Acad Sci U S A 109: 4479-84

Wu MJ, Chen YS, Kim MR, Chang CC, Gampala S, Zhang Y, Wang Y, Chang CY, Yang JY, Chang CJ (2019) Epithelial-Mesenchymal Transition Directs Stem Cell Polarity via Regulation of Mitofusin. Cell Metab 29: 993-1002 e6

Xie Q, Wu Q, Horbinski CM, Flavahan WA, Yang K, Zhou W, Dombrowski SM, Huang Z, Fang X, Shi Y, Ferguson AN, Kashatus DF, Bao S, Rich JN (2015) Mitochondrial control by DRP1 in brain tumor initiating cells. Nat Neurosci 18: 501-10

Zerjatke T, Gak IA, Kirova D, Fuhrmann M, Daniel K, Gonciarz M, Muller D, Glauche I, Mansfeld J (2017) Quantitative Cell Cycle Analysis Based on an Endogenous All-in-One Reporter for Cell Tracking and Classification. Cell Rep 19: 1953-1966

Zhang H, Menzies KJ, Auwerx J (2018) The role of mitochondria in stem cell fate and aging. Development 145

Zhao Q, Yan S, Lu J, Parker DJ, Wu H, Sun Q, Crossman DK, Liu S, Wang Q, Sesaki H, Mitra K, Liu K, Jiao K (2021) Mitochondrial Fission Regulates Transcription of Ribosomal Protein Genes in Embryonic Hearts
bioRxiv 2021.02.10.430627; doi: https://doi.org/10.1101/2021.02.10.430627

Zhong X, Cui P, Cai Y, Wang L, He X, Long P, Lu K, Yan R, Zhang Y, Pan X, Zhao X, Li W, Zhang H, Zhou Q, Gao P (2019) Mitochondrial Dynamics Is Critical for the Full Pluripotency and Embryonic Developmental Potential of Pluripotent Stem Cells. Cell Metab 29: 979-992 e4

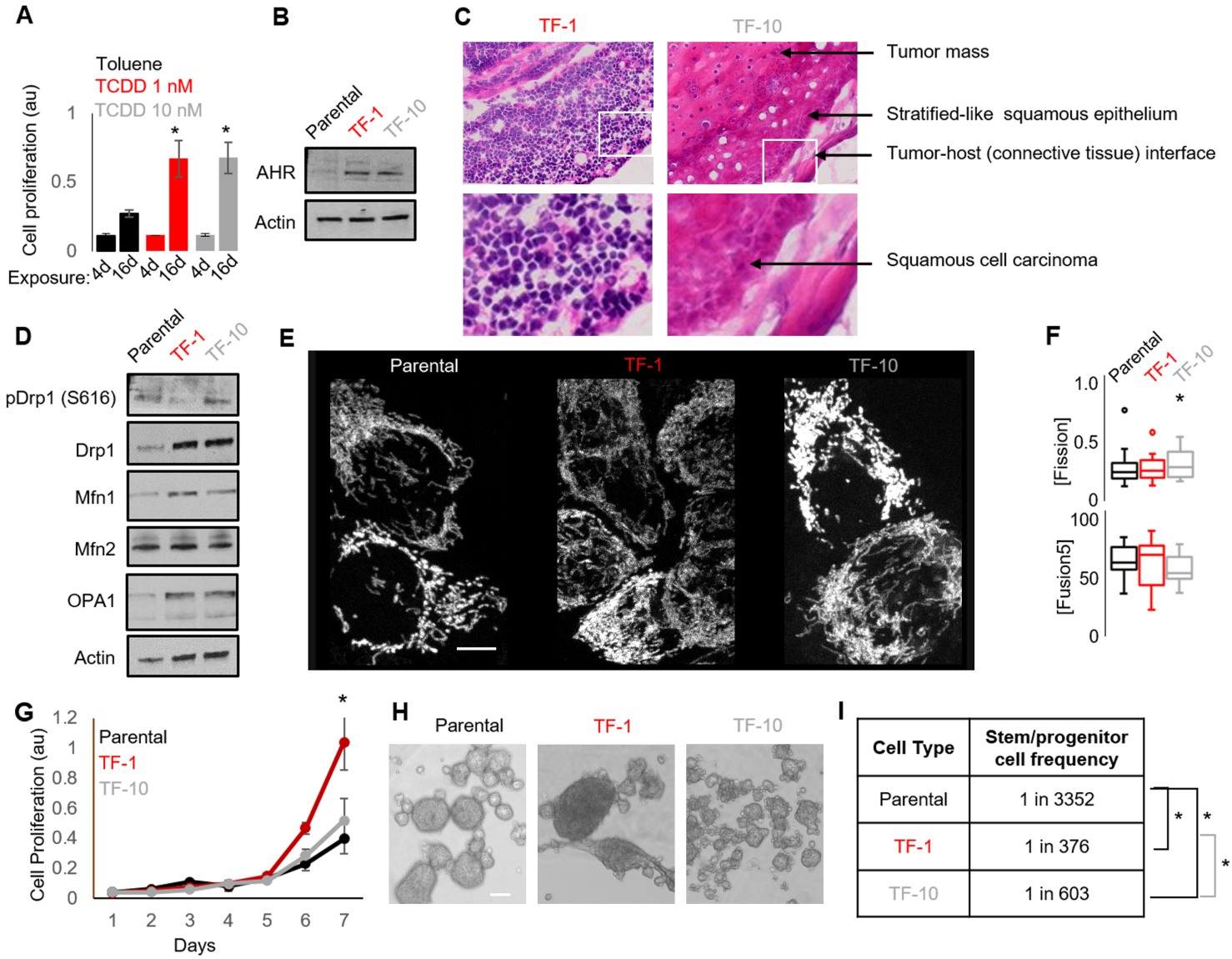
A
Toluene
TCDD 1 nM
TCDD 10 nM
Cell proliferation (au)
1
0.5
0
*
*
Exposure: 4d 16d 4d 16d 4d 16d
B
Parental
TF-1
TF-10
AHR
Actin
C
TF-1
TF-10
Tumor mass
Stratified-like squamous epithelium
Tumor-host (connective tissue) interface
Squamous cell carcinoma
D
Parental
TF-1
TF-10
pDrp1 (S616)
Drp1
Mfn1
Mfn2
OPA1
Actin
E
Parental
TF-1
TF-10
F
Parental
TF-1
TF-10
[Fission]
1.0
0.5
0
*
[Fusion5]
100
50
0
G
Cell Proliferation (au)
1.2
1
0.8
0.6
0.4
0.2
0
Parental
TF-1
TF-10
*
1 2 3 4 5 6 7
Days
H
Parental
TF-1
TF-10
I
Cell Type | Stem/progenitor cell frequency
Parental | 1 in 3352
TF-1 | 1 in 376
TF-10 | 1 in 603
*
*
*

Figure. 1

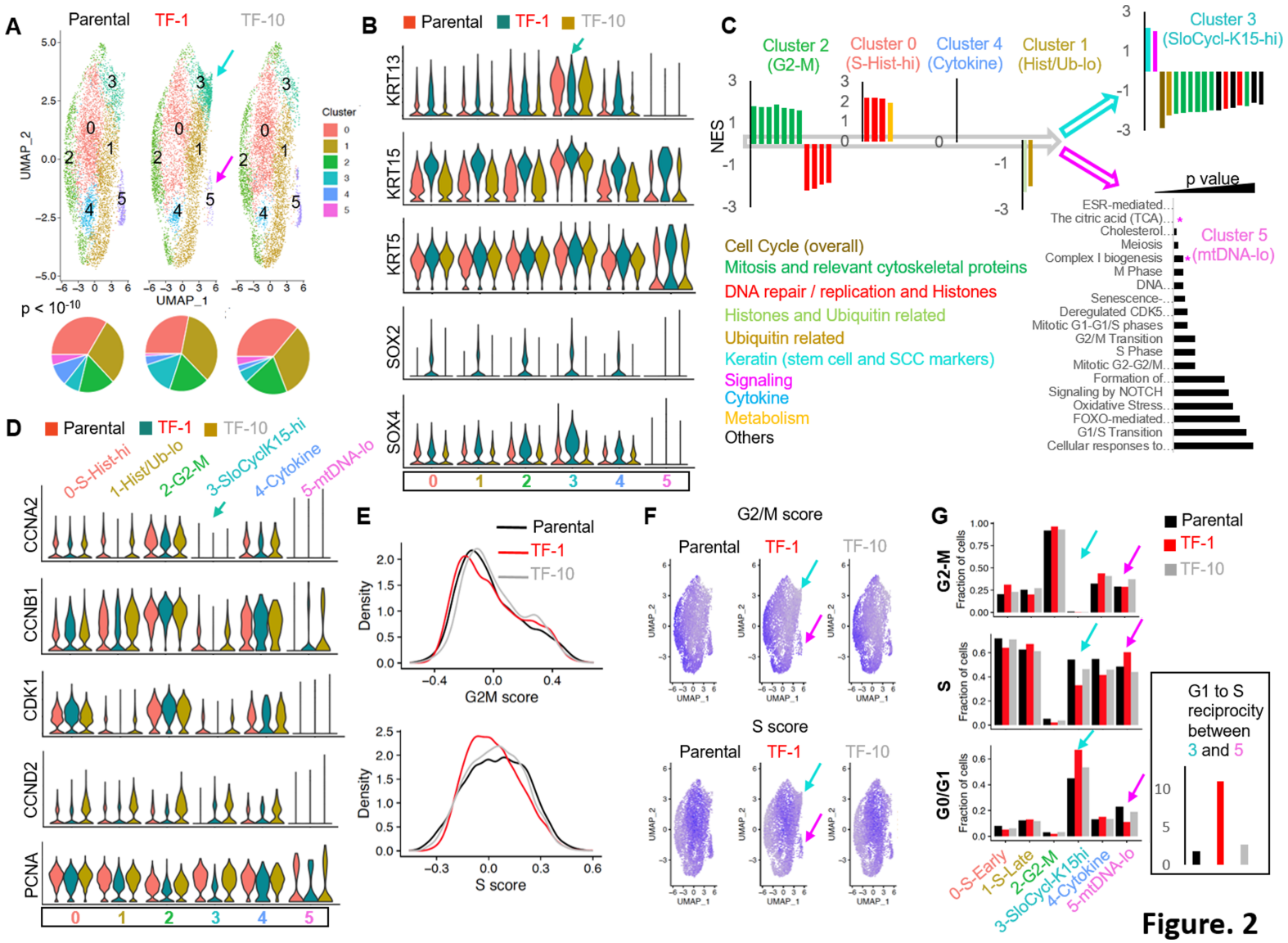
A
Parental
TF-1
TF-10
UMAP_2
UMAP_1
Cluster
p < 10-10
B
Parental
TF-1
TF-10
KRT13
KRT15
KRT5
SOX2
SOX4
C
Cluster 2 (G2-M)
Cluster 0 (S-Hist-hi)
Cluster 4 (Cytokine)
Cluster 1 (Hist/Ub-lo)
Cluster 3 (SloCycl-K15-hi)
Cluster 5 (mtDNA-lo)
NES
p value
Cell Cycle (overall)
Mitosis and relevant cytoskeletal proteins
DNA repair / replication and Histones
Histones and Ubiquitin related
Ubiquitin related
Keratin (stem cell and SCC markers)
Signaling
Cytokine
Metabolism
Others
ESR-mediated...
The citric acid (TCA)...
Cholesterol...
Meiosis
Complex I biogenesis
M Phase
DNA...
Senescence-...
Deregulated CDK5...
Mitotic G1-G1/S phases
G2/M Transition
S Phase
Mitotic G2-G2/M...
Formation of...
Signaling by NOTCH
Oxidative Stress...
FOXO-mediated...
G1/S Transition
Cellular responses to...
D
Parental
TF-1
TF-10
0-S-Hist-hi
1-Hist/Ub-lo
2-G2-M
3-SloCyclK15-hi
4-Cytokine
5-mtDNA-lo
CCNA2
CCNB1
CDK1
CCND2
PCNA
E
Parental
TF-1
TF-10
Density
G2M score
S score
F
G2/M score
S score
Parental
TF-1
TF-10
UMAP_2
UMAP_1
G
Parental
TF-1
TF-10
G2-M
S
G0/G1
Fraction of cells
G1 to S reciprocity between 3 and 5
0-S-Early
1-S-Late
2-G2-M
3-SloCycl-K15hi
4-Cytokine
5-mtDNA-lo

Figure. 2

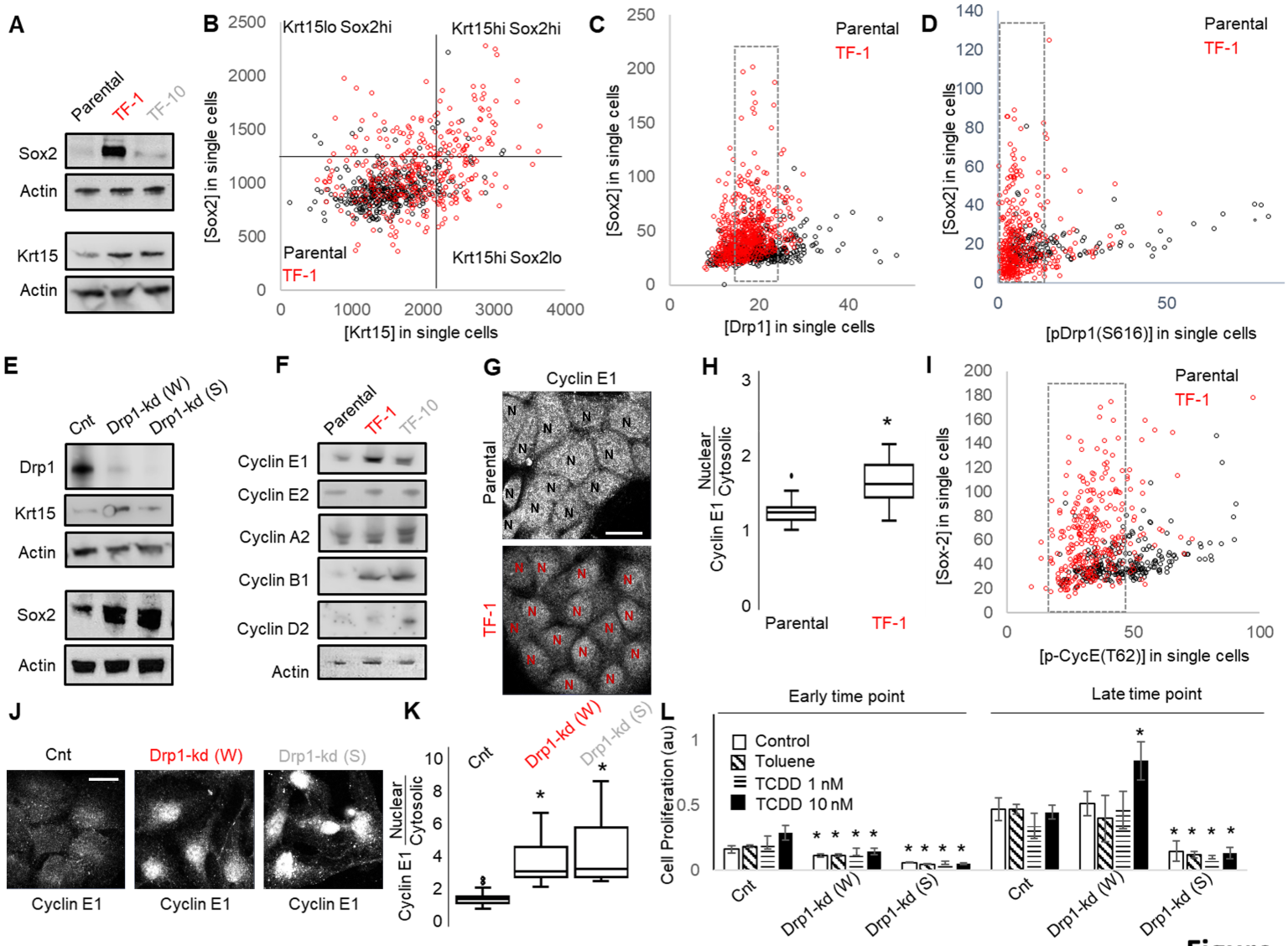
A
Parental
TF-1
TF-10
Sox2
Actin
Krt15
Actin
B
Krt15lo Sox2hi
Krt15hi Sox2hi
Krt15hi Sox2lo
Parental
TF-1
[Sox2] in single cells
[Krt15] in single cells
C
Parental
TF-1
[Sox2] in single cells
[Drp1] in single cells
D
Parental
TF-1
[Sox2] in single cells
[pDrp1(S616)] in single cells
E
Cnt
Drp1-kd (W)
Drp1-kd (S)
Drp1
Krt15
Actin
Sox2
Actin
F
Parental
TF-1
TF-10
Cyclin E1
Cyclin E2
Cyclin A2
Cyclin B1
Cyclin D2
Actin
G
Cyclin E1
Parental
TF-1
H
Nuclear / Cytosolic
Cyclin E1
Parental
TF-1
I
Parental
TF-1
[Sox-2] in single cells
[p-CycE(T62)] in single cells
J
Cnt
Drp1-kd (W)
Drp1-kd (S)
Cyclin E1
Cyclin E1
Cyclin E1
K
Cnt
Drp1-kd (W)
Drp1-kd (S)
Nuclear / Cytosolic
Cyclin E1
L
Early time point
Late time point
Control
Toluene
TCDD 1 nM
TCDD 10 nM
Cell Proliferation (au)
Cnt
Drp1-kd (W)
Drp1-kd (S)
Cnt
Drp1-kd (W)
Drp1-kd (S)

Figure. 3

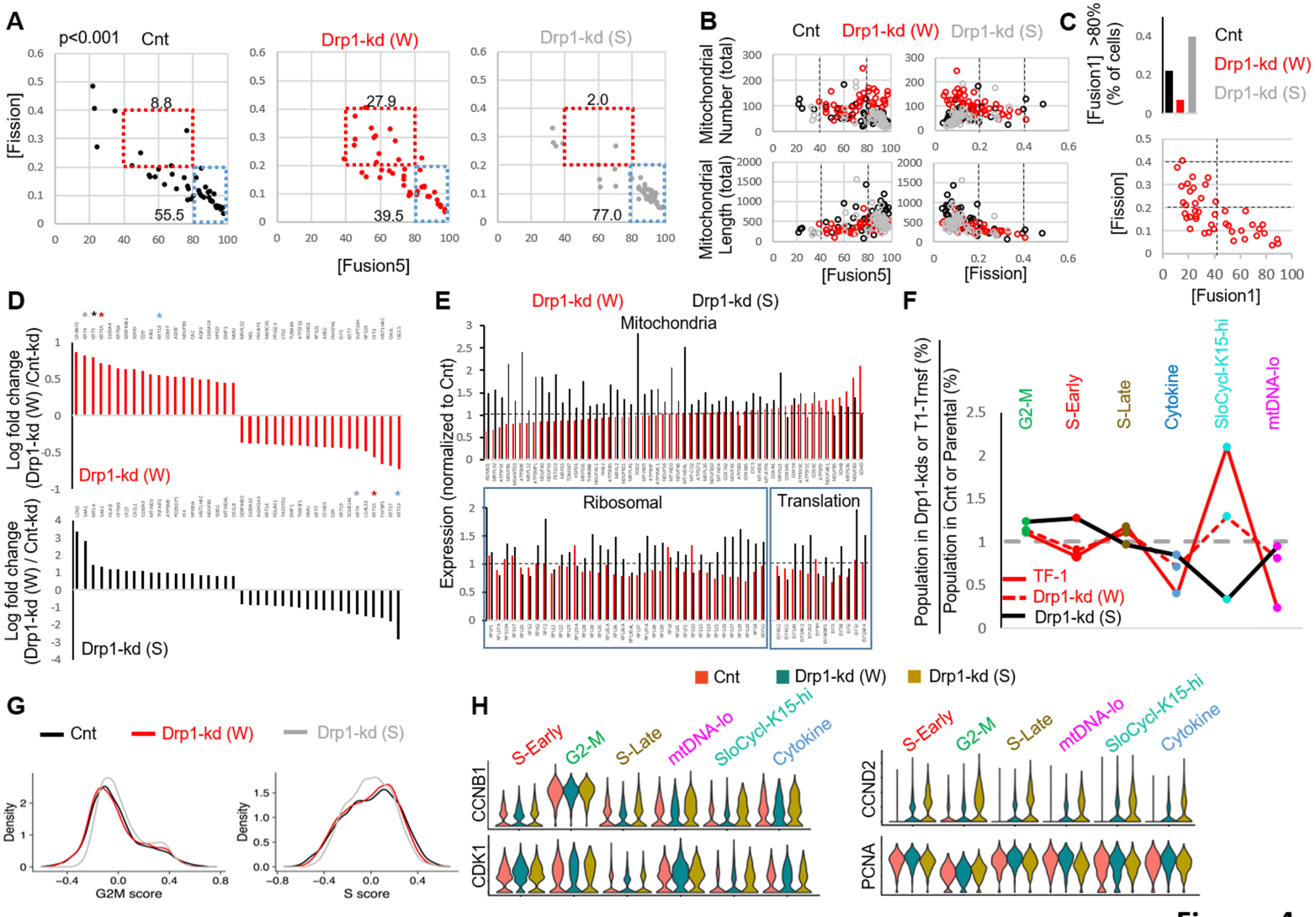
A
p<0.001
Cnt
Drp1-kd (W)
Drp1-kd (S)
[Fission]
[Fusion5]
8.8
55.5
27.9
39.5
2.0
77.0
B
Cnt
Drp1-kd (W)
Drp1-kd (S)
Mitochondrial Number (total)
Mitochondrial Length (total)
[Fusion5]
[Fission]
C
[Fusion1] >80% (% of cells)
Cnt
Drp1-kd (W)
Drp1-kd (S)
[Fission]
[Fusion1]
D
Log fold change (Drp1-kd (W) /Cnt-kd)
Drp1-kd (W)
Log fold change (Drp1-kd (W) / Cnt-kd)
Drp1-kd (S)
E
Drp1-kd (W)
Drp1-kd (S)
Mitochondria
Ribosomal
Translation
Expression (normalized to Cnt)
F
Population in Drp1-kds or T1-Trnsf (%)
Population in Cnt or Parental (%)
G2-M
S-Early
S-Late
Cytokine
SloCycl-K15-hi
mtDNA-lo
TF-1
Drp1-kd (W)
Drp1-kd (S)
G
Cnt
Drp1-kd (W)
Drp1-kd (S)
Density
G2M score
S score
H
Cnt
Drp1-kd (W)
Drp1-kd (S)
S-Early
G2-M
S-Late
mtDNA-lo
SloCycl-K15-hi
Cytokine
CCNB1
CDK1
CCND2
PCNA

Figure. 4

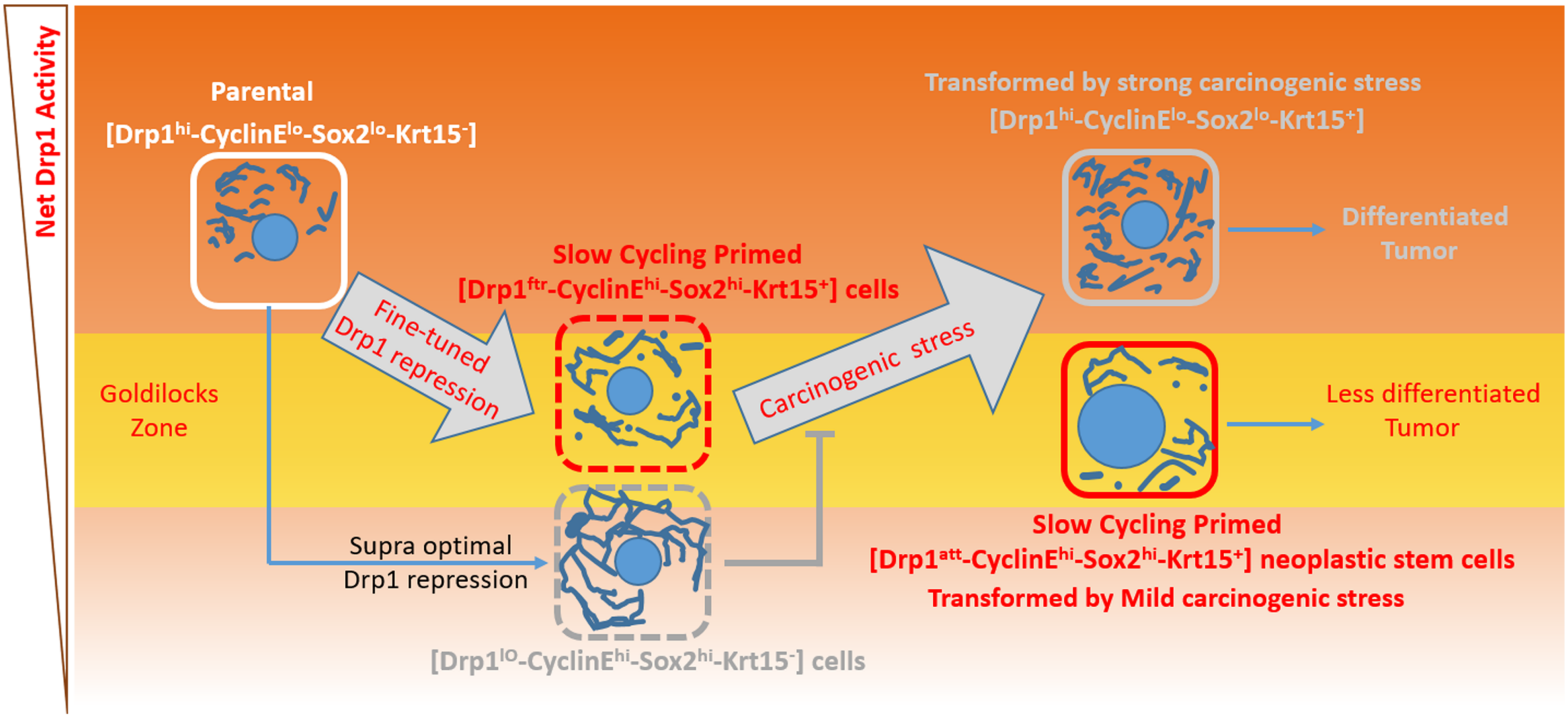
Net Drp1 Activity
Parental
[Drp1hi-CyclinElo-Sox2lo-Krt15-]
Fine-tuned
Drp1 repression
Slow Cycling Primed
[Drp1ftr-CyclinEhi-Sox2hi-Krt15+] cells
Carcinogenic stress
Transformed by strong carcinogenic stress
[Drp1hi-CyclinElo-Sox2lo-Krt15+]
Differentiated
Tumor
Goldilocks
Zone
Less differentiated
Tumor
Supra optimal
Drp1 repression
Slow Cycling Primed
[Drp1att-CyclinEhi-Sox2hi-Krt15+] neoplastic stem cells
Transformed by Mild carcinogenic stress
[Drp1lO-CyclinEhi-Sox2hi-Krt15-] cells

Figure. 5

A

Cells Injected	Tumor incidence	Tumor volume
Parental	0/9	N.A.
TF-1	#1/9	188.1 #363.1
TF-10	3/9	287.9 ± 173

B

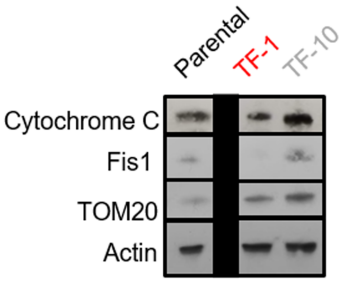

Extended Fig. 1

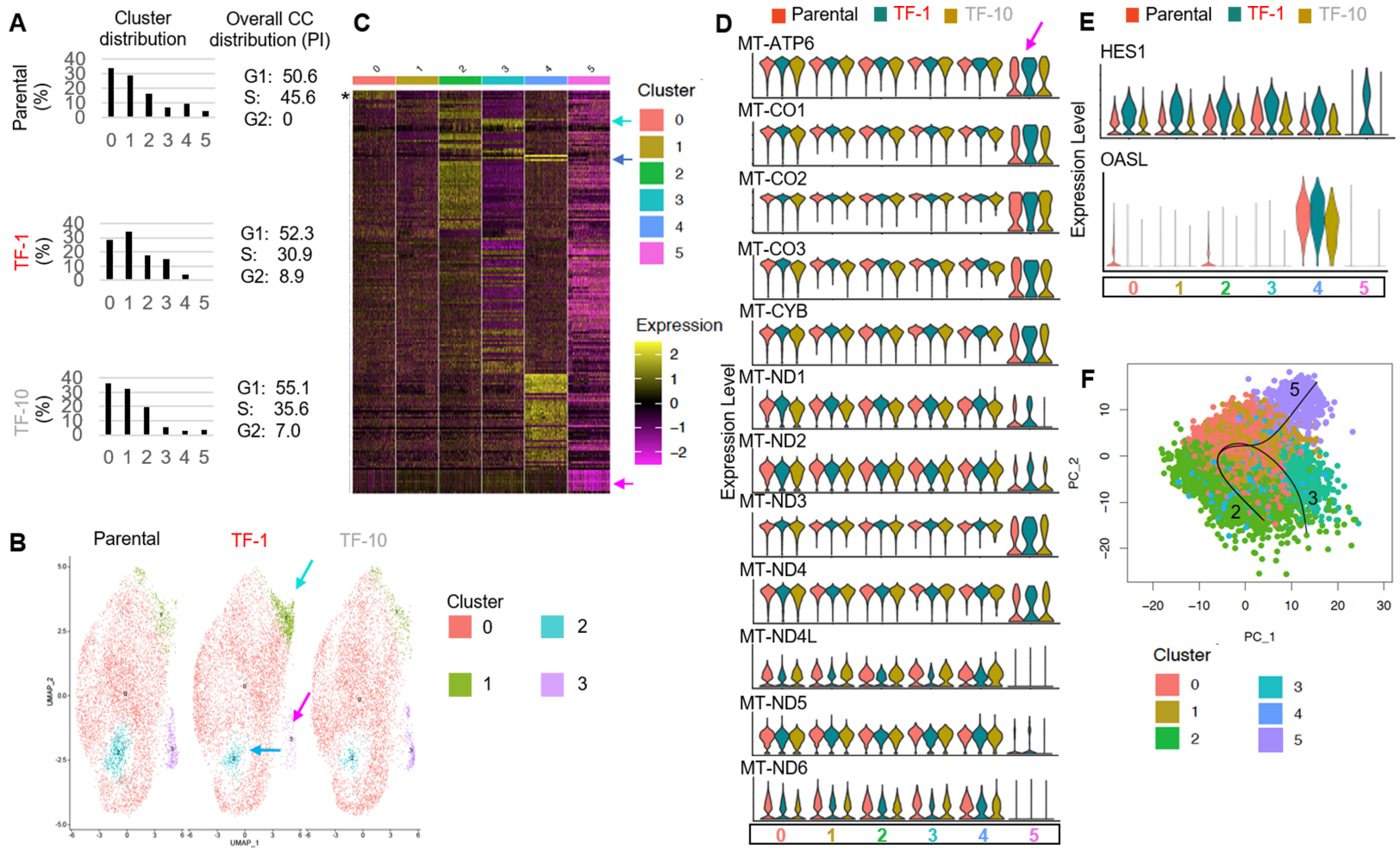

Extended Fig. 2

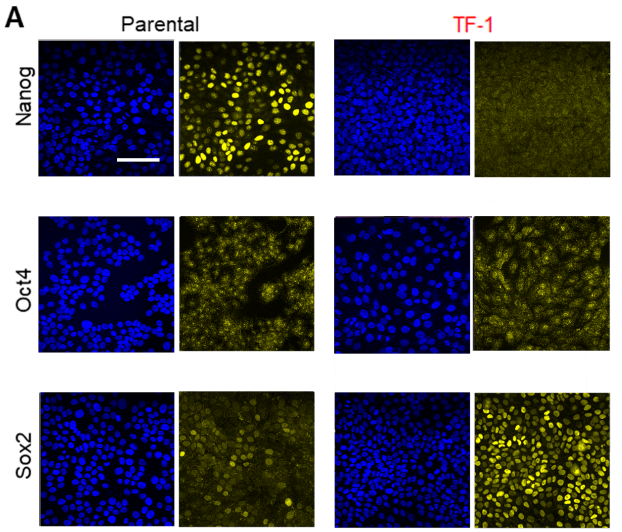

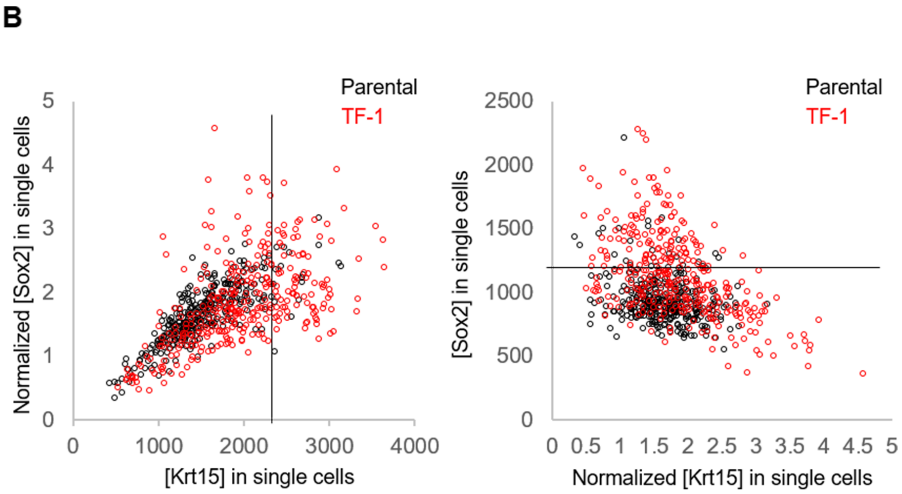

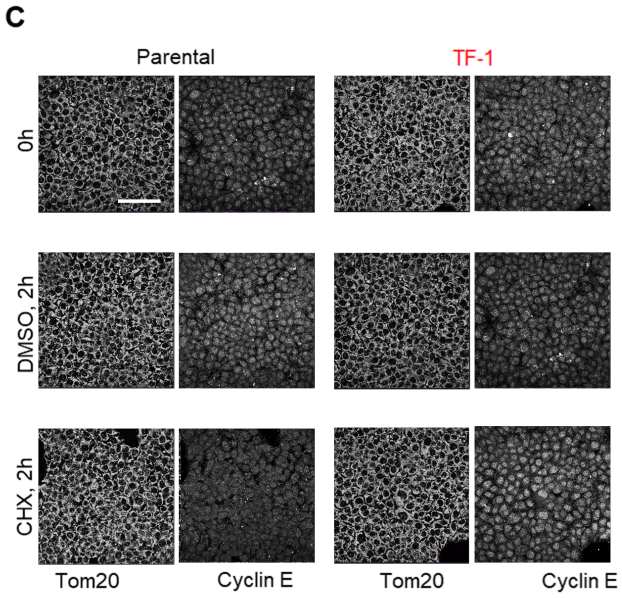

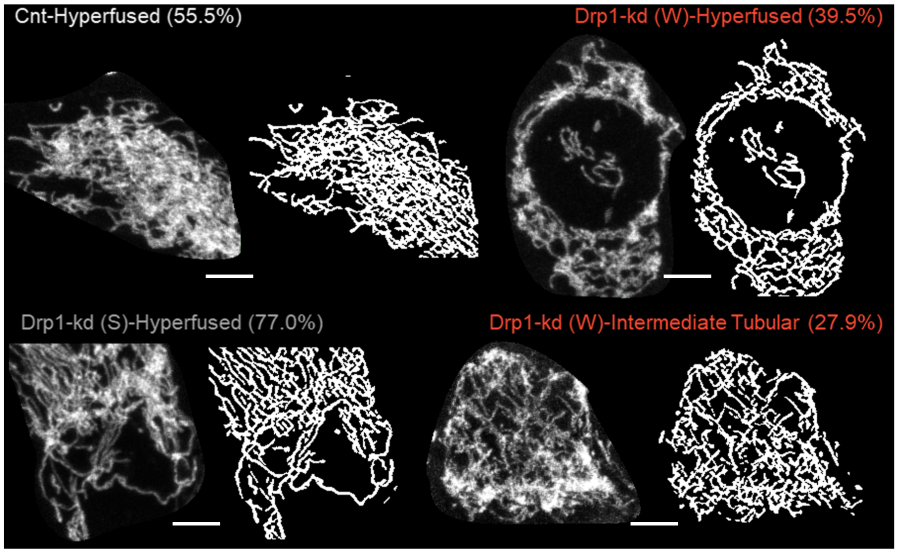

Extended Fig. 3

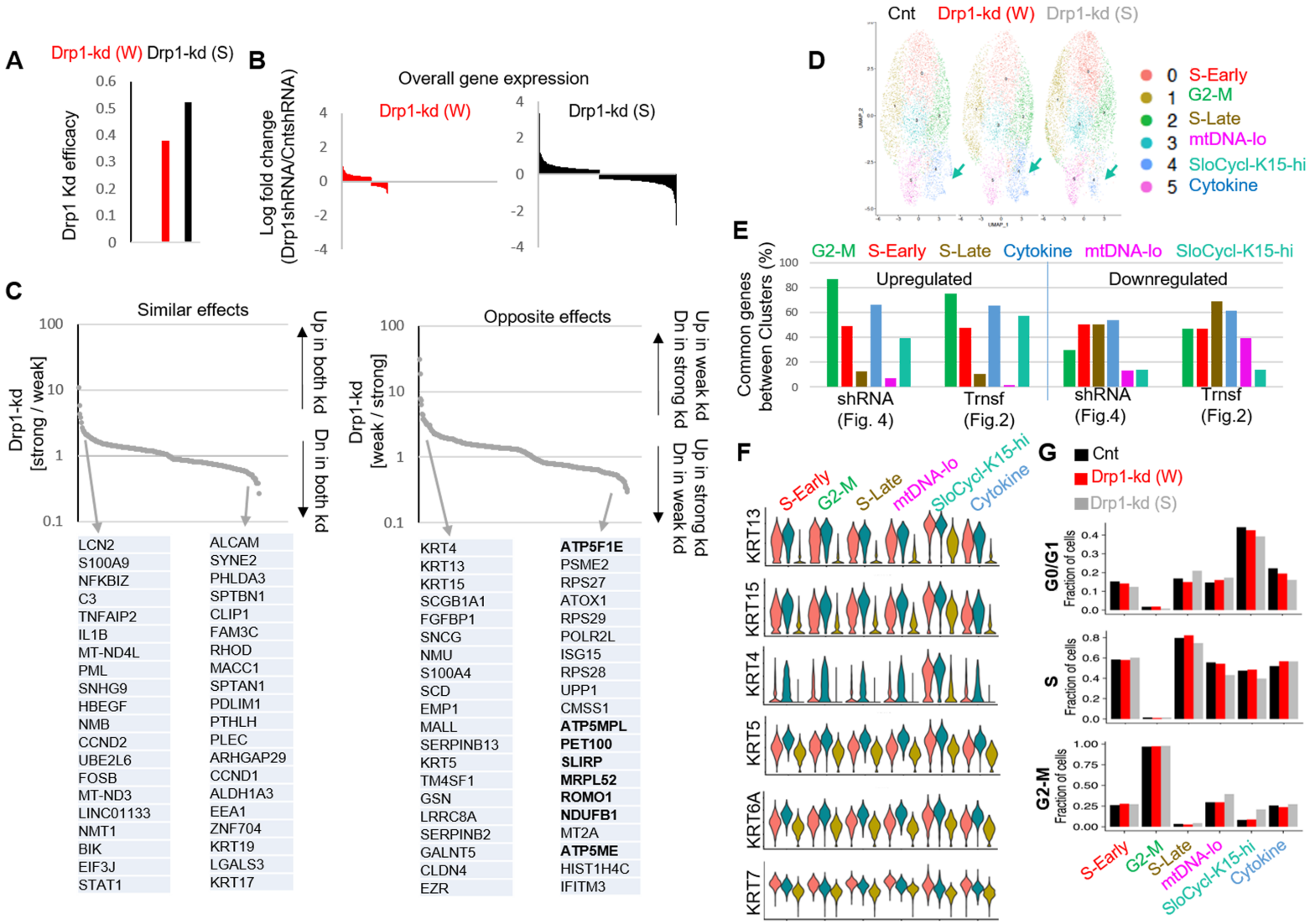

Extended Fig. 4

795 **EXTENDED FIGURE LEGENDS:**

796 **Extended Figure 1. A)** Quantification of incidence and volume of xenograft tumors
797 formed by TF-1 and TF-10 HaCaT cells; # indicates presence of a distant tumor. **B)**
798 Immunoblot analyses of Cytochrome C, Fis1, Tom20 and actin (loading control) in
799 Parental and TF-1 and TF-10 HaCaT cells.

800 **Extended Figure 2. A)** Bar plot showing the percentage distribution of the clusters (0-5)
801 in each of the cell populations identified by scRNA-seq analyses of Parental, TF-1 and
802 TF-10 HaCat cells (left); numbers show cell cycle distribution from flowcytometry
803 analyses of PI stained cells in the corresponding population (right). **B)** UMAP plot of
804 scRNA-seq derived clusters (0-5) of Parental, TF-1 and TF-10 HaCaT cells obtained
805 with minimum cluster resolution; color coded arrows point the major change in cluster
806 distribution in transformed cells. **C)** Heat map of statistically significant marker genes for
807 the color-coded clusters (0-5) of Parental, TF-1 and TF-10 HaCaT cells; color coded
808 arrows point to the top most marker gene in the 3 clusters that are have different
809 distribution between the Parental and transformed populations; color index shows log
810 fold change; * marks the Histone gene cluster. **D)** Violin plots depicting expression of
811 the mt-DNA genes in the named scRNA-seq derived cell clusters in the Parental, TF-1
812 and TF-10 HaCaT cells. **E)** Violin plots depicting expression of HES1 and OASL genes
813 in the named scRNA-seq derived cell clusters in the Parental, TF-1 and TF-10 HaCaT
814 cells. **F)** PCA plot of trajectory analyses of the scRNA-seq derived cell clusters in the
815 Parental, TF-1 and TF-10 HaCaT cells.

816 **Extended Figure 3. A)** Representative confocal micrographs of immunostained
817 Parental and TF-1 HaCaT cells showing endogenous expression of Oct4, Nanog and
818 Sox2; blue depicting nuclear staining with Hoechst. **B)** Dot plot of [Sox2] and [Krt15]
819 obtained from confocal micrographs of co-immunostained Parental and TF-1 HaCaT
820 cells; [Sox2] levels normalized to the minimum in the respective population (left) and
821 [Krt15] levels normalized to the minimum in the respective population (right); black lines
822 demarcate levels of Sox2 and Krt15 as determined from the normalized signal of the
823 other. **C)** Representative confocal micrographs of Parental and TF-1 HaCaT cells
824 showing endogenous expression of Tom20 and Cyclin E1 after 2 hours incubation with

825 DMSO or Cychloheximide, with the pre-incubation time point (0h) as control. **D)**
826 Representative maximum intensity projections (MIP) of confocal optical sections
827 (micrograph) and the corresponding MitoGraph generated binary images (binary) for
828 quantifying [Fission] and [Fusion1/5] metrics of the Parental HaCaT cells expressing
829 non-targeted shRNA (Cnt), strong (S) or weak (W) Drp1 shRNA; the cells represent
830 populations in colored boxes in Fig. 4A while the number depicts their abundance in
831 percentage. Scale bar depicts 100 μm (A, C) or 15 μm (D).

832 **Extended Figure 4. A)** Bar plot showing the knockdown efficiency of strong (S) or weak
833 (W) Drp1 shRNA expressed as ratio of Drp1 transcript levels in the knockdown HaCaT
834 and that of the cells expressing the non-targeted shRNA control. **B)** Bar plot showing
835 log fold change of overall gene expression of Parental HaCaT cells expressing strong
836 (S) or weak (W) Drp1 shRNA with respect to those expressing the non-targeted shRNA
837 (Cnt). **C)** Plots showing ratio of the expression of covered genes between the Parental
838 HaCaT cells expressing strong (S) or weak (W) Drp1 shRNA; "Similar effects" showing
839 ratio of increase or decrease in the (S) Drp1 shRNA over the (W) Drp1 shRNA (back
840 arrows in left panel), while opposite effects showing opposite trends in genes as
841 labelled in the arrows (back arrows right panel); grey arrows point to the top 20 genes of
842 each category. **D)** UMAP plot of scRNA-seq based clusters (0-5) of Parental HaCaT
843 cells expressing non-targeted shRNA (Cnt), strong (S) or weak (W) Drp1 shRNA; arrow
844 pointing the SloCyc-Krt15-hi cluster (note color coding is not same as the one presented
845 in Fig. 2). **E)** Bar plot showing percentage of statistically significant common genes
846 (Upregulated or Downregulated) between color coded clusters obtained with the
847 scRNA-seq data set of parental and transformed HaCaT cells (Fig. 2) and that of
848 parental expressing control or Drp1 shRNAs (Fig. 4); same color coding is maintained
849 between the two data sets. **F)** Violin plots depicting expression of Krt13, Krt15, Krt4,
850 Krt5, Krt6A, Krt7 genes in the named scRNA-seq based cell clusters in the Parental
851 HaCaT cells expressing non-targeted shRNA (Cnt), strong (S) or weak (W) Drp1
852 shRNA. **G)** Bar plot showing fraction of cells in G2-M, S and G0/G1, computed from
853 main Fig. 4G, in the functionally categorized clusters in the Parental cells expressing
854 non-targeted shRNA (Cnt), strong (S) or weak (W) Drp1 shRNA.
855